Optics and Lasers in Engineering 143 (2021) 106622

Contents lists available at ScienceDirect

Optics and Lasers in Engineering

journal homepage: www.elsevier.com/locate/optlaseng

Review

# Calibration of fringe projection profilometry: A comparative review

Shijie Feng[a,b,c], Chao Zuo[a,b,c,*], Liang Zhang[a,b,c], Tianyang Tao[a,b,c], Yan Hu[a,b,c], Wei Yin[a,b,c], Jiaming Qian[a,b,c], Qian Chen[a,b,*]

[a] School of Electronic and Optical Engineering, Nanjing University of Science and Technology, No. 200 Xiaolingwei Street, Nanjing, Jiangsu Province 210094, China
[b] Jiangsu Key Laboratory of Spectral Imaging & Intelligent Sense, Nanjing, Jiangsu Province 210094, China
[c] Smart Computational Imaging Laboratory (SCILab), Nanjing University of Science and Technology, Nanjing, Jiangsu Province 210094, China

ARTICLE INFO

*Keywords:*
Fringe projection
Calibration
3D measurement
Structured light
Phase retrieval

ABSTRACT

Fringe projection profilometry is widely used for three-dimensional (3D) measurements. System calibration is crucial to fringe projection systems, since it determines how the phase is converted into 3D geometry. Many methods and studies on calibration have been presented in the last few years. However, a comparative overview on the accuracy and the implementation details is still lacking. In this work, we present a review of some of the most used calibration methods. First, the basic principles are reviewed. Then, both quantitative and qualitative comparative experiments are implemented to show the advantages and constraints of each method. Further, a number of factors that may affect the performance of the calibration are discussed. Sample codes are available for better comprehension and a quick start of these methods.

## 1. Introduction

Three-dimensional (3D) shape information plays an essential role in many fields, e.g., industrial manufacturing [1–3], geomaterials [4], biomechanics [5], optical engineering [6–9], and computer vision [10–14]. Coordinate measuring machines (CMMs), time of flight (ToF) cameras, stereo vision sensors, and structured light illumination systems are widely used for 3D shape measurements of objects, ranging in size from tens of centimeters to one or two meters. The CMM measures objects through point-by-point physical contacts and is widely applied to industrial inspections [15]. It has the advantages of high accuracy and being insensitive to reflective materials. Due to point-by-point detections, however, the measurement efficiency is not high. ToF cameras measure the distance according to the time when a light emits and returns from measured objects. They are extensively employed in developing 3D sensors for unmanned vehicles and mobile devices [16]. Although ToF cameras can obtain 3D data at high speed, their resolution is relatively low. The stereo vision imitates the depth-sensing process of human eyes and estimates the distance by deriving the disparity of the same object point in different views [17]. Despite being able to measure a full field at a time with high resolution, it is fragile for uniform or periodic textures.

Structured light illumination techniques replace one of the cameras in the stereo vision with a projector. By illuminating measured surfaces with pre-designed patterns, the structured light illumination is more robust than the stereo vision [18–24]. In the structured light illumination, projected patterns have various structures, such as sinusoidal fringe images [25–32], random speckles [33–35], and some custom-made structures [36–39]. Approaches that use fringe patterns are known as the fringe projection profilometry, which has the advantages of high-resolution and high-accuracy 3D measurements. The fringe projection profilometry extracts the phase information from captured sinusoidal fringes and converts the phase into 3D reconstructions.

In fringe projection, there are several steps to obtain a 3D reconstruction. First, fringe patterns are projected onto measured objects and are captured from a different viewpoint. The system nonlinearity [40–44] and the limited dynamic range of fringe projection systems [45–50] may destroy the captured sinusoidal patterns. For accurate 3D measurements, these effects should be compensated. Then, fringe analysis approaches are used to extract wrapped phase maps from the captured images [51–61]. Next, the wrapped phase is unwrapped to get a continuous phase distribution [62–67]. The last step is to convert the unwrapped phase into 3D coordinates. In this step, the system calibration calculates parameters that determine how the phase converts to the 3D reconstruction. System calibration is the key to fringe projection, as the quality of final 3D reconstructions relies on how accurately the system coefficients have been calibrated.

In this work, we mainly focus on the calibration methods for typical fringe projection systems that consist of a single camera and a single projector. For systems with more than one cameras or projectors, the way of calibration is an extension of the methods discussed here. In general, the calibration models can be roughly classified into two groups: phase-height models and triangular stereo models. In the phase-height models,

* Corresponding authors.
*E-mail addresses:* shijiefeng@njust.edu.cn (S. Feng), zuochao@njust.edu.cn (C. Zuo), chenqian@njust.edu.cn (Q. Chen).

https://doi.org/10.1016/j.optlaseng.2021.106622
Received 20 August 2020; Received in revised form 8 February 2021; Accepted 14 March 2021

the object's height is measured relative to a reference plane. The height is a function of phase. Usually, the phase-height function depends on how the camera and the projector are arranged. In early phase-height models [53], the optical axis of the camera is supposed to be parallel to that of the projector. Also, the distance to the reference plane should be the same for the camera and the projector. However, it is hard to meet the geometric constraints fully in practice. Then, researchers proposed to remove the assumption of the parallel optical axes [68–79]. With the relief on the geometric constraint, the flexibility of the fringe projection system increases. However, the tilted projector illuminates the reference plane with uneven fringe patterns, which increases the complexity of the mapping from phase to height. To further improve the flexibility, many generalized phase-height models have been investigated [80–95]. The advantage is that one can arrange the camera and the projector freely without considering the geometric constraints.

Instead of converting the phase into the height directly, triangular stereo models exploit the phase in a different way for 3D reconstructions. Their idea stems from the stereo vision model, where an object point is measured by matching its image in different camera views. In triangular stereo models, both the camera and the projector are calibrated. The phase serves as objects' temporary texture that facilitates the search of corresponding points in the views of the camera and the projector. In these models, the image projection is regarded as a reverse process of image capture. Therefore, the projector is utilized as an inverse camera, which is able to see the measurement point with the assistance of the phase. Thus, the projector can be calibrated in the same way that one calibrates a camera. To make the projector visible, a calibrated camera can assist the projector to find necessary feature points for calibration [96–101]. However, the error of the camera calibration may propagate and affect the accuracy of the projector calibration. To handle this issue, projector calibration approaches without requiring the camera calibration have been proposed [100,102–106,106–127]. They can avoid the influence of the camera calibration error on the projector calibration, thus increasing the accuracy of the system calibration. Calibration techniques for microscopic fringe projection profilometry also utilize the triangular stereo model. However, the imaging model is different due to the usage of telecentric lenses. For the calibration of a microscopic fringe projection system, readers may refer to Refs. [128–132].

Some calibration methods have presented phase-height models where the camera is calibrated [88,133–146]. In traditional phase-height models, a reference plane should be measured at several known heights. The reference plane's accurate movement is performed by using expensive high-precision displacement stages or gauge blocks. However, the displacement stage is no longer necessary if the camera is calibrated. Specifically, the camera is calibrated by using a calibration board placing arbitrarily in front of it. The calibration board at the first orientation can be treated as a reference plane. The board at the rest orientations can be used as the reference planes at different heights. The rotation and the translation between each calibration board's orientation can be estimated once the camera has been calibrated. Thus, the 3D positions of the feature points on the calibration board at the rest orientations can be transformed into the coordinate system determined by the calibration board's first position. Each feature point's height can then be obtained by calculating its distance to the reference plane fitted by feature points of the calibration board at the first position. In this way, the displacement stage is no longer needed in these phase-height models.

As can be seen, there are various calibration methods in fringe projection profilometry. However, researchers especially beginners often spend large amounts of time searching for a proper calibration approach. Despite significant improvements and wide applications, there are few published works regarding the comparison of calibration methods. In this work, we select several representative calibration methods for comparison. The selected calibration models are the linear phase-height model, the linear inverse phase-height model, the polynomial phase-height model, the governing equation based phase-height model, and the triangular stereo model where the projector is calibrated without the assistance of a calibrated camera.

First, we introduce basic theories of the phase computation and the phase unwrapping in fringe projection. Then, the principles of the selected calibration models are described. Next, these models are evaluated by one qualitative and three quantitative experiments. In the first quantitative experiment, we compare the accuracy of reconstructed planes at different heights which are known in advance. In the second quantitative experiment, we calibrate our system by limiting the movement of calibration tools (e.g., the reference plane and the calibration board) within half of the measurement volume but test the plane's reconstruction accuracy in the full range. This experiment aims to show each calibration method's sensitivity to the measurement volume that is not calibrated. In the third quantitative experiment, phase-shifting algorithms of different steps are used to study the effect of a phase retrieval algorithm on the system calibration. In the qualitative experiment, the performance of the selected model is compared through measurements of a complex plaster model. After experimental evaluations, we further discuss these techniques from eight aspects, including the type of retrieved 3D data, the extraction of feature points for calibration, the effect of the system nonlinearity on calibration, the selection of an appropriate calibration method for 3D measurements out of the lab, the selection of the proper volume to be calibrated, potentials for real-time 3D measurements, and how to reduce the cost of calibration tools. It is noteworthy that sample codes of these compared methods are provided with this paper, which would facilitate a quick start of these methods. We hope this work would provide useful hints for readers to find the desired calibration method rapidly.

## 2. Phase calculation

A basic fringe projection system consists of a projector and a camera, as shown in Fig. 1. The projector illuminates measured objects with pre-designed patterns, and the camera captures the patterns that are distorted by the object's surface from a different viewpoint. A wrapped phase map can be extracted from the captured fringe patterns by fringe analysis techniques, e.g., single-shot methods [51,53,57–59] or multi-shot methods [52]. Here, we take the $N$-step phase-shifting algorithm as an example since it is a representative multi-shot method and has the advantage of high accuracy. The captured fringe images can be written as

$$I_n(x,y) = I_a(x,y) + I_b(x,y)\cos\left[\varphi(x,y) - 2\pi n/N\right] \tag{1}$$

where $n \in [0, N-1]$, $I_a$ is the background image, $I_b$ the modulation image and $(x, y)$ the camera pixel coordinate. $\varphi$ is the phase that can be calculated by

$$\varphi(x,y) = \tan^{-1}\frac{\sum_{n=0}^{N-1} I_n(x,y)\sin(2\pi n/N)}{\sum_{n=0}^{N-1} I_n(x,y)\cos(2\pi n/N)} \tag{2}$$

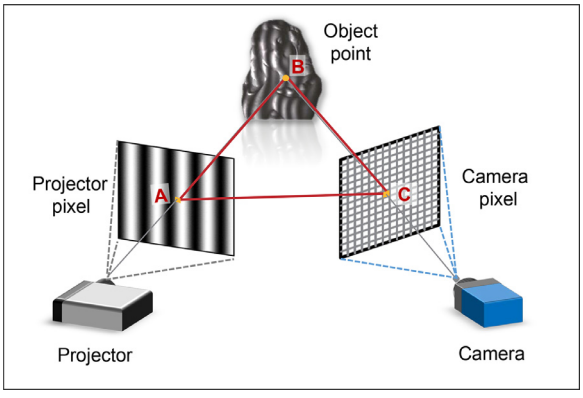


**Fig. 1.** Schematic of 3D measurements by fringe projection profilometry.

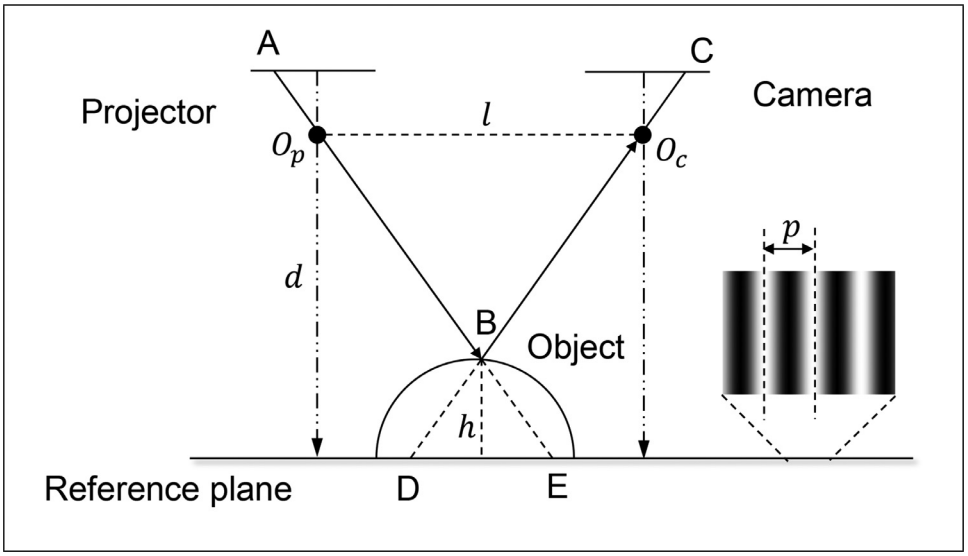


**Fig. 2.** Schematic of the classic phase-height model where the optical axes of the camera and the projector are parallel.

The phase obtained by Eq. (2) is wrapped within $-\pi$ to $\pi$. To retrieve a continuous phase distribution, phase unwrapping is carried out by

$$\phi(x,y) = \varphi(x,y) + 2\pi K(x,y) \tag{3}$$

where $\phi$ is the unwrapped phase and $K$ the fringe order that is computed by the phase unwrapping algorithms [62,64,65,147,148]. Once the fringe projection system has been calibrated, the unwrapped phase $\phi$ can be converted into the 3D reconstruction.

## 3. Principles of system calibration

Over the past few decades, various calibration methods have been proposed. They can be roughly categorized into two groups: phase-height models and triangular stereo models. In the phase-height models, a reference plane with height $h(x,y) = 0$ is required. The object's height is then measured relative to the position of the reference plane. The phase plays a role that relates to the height directly. Specifically, the height can be a function of a phase difference, which is the difference between the object's phase and the reference plane's phase, i.e., $h(x,y) = f(x,y,\Delta\phi,\boldsymbol{\theta})$, where $\boldsymbol{\theta}$ is a vector that consists of parameters to be calibrated. Alternatively, the height can also be the function of the object's phase itself, i.e., $h(x,y) = f(x,y,\phi,\boldsymbol{\theta})$.

In a triangular stereo model, however, the phase is not converted into the height directly but instead acts as a bridge to connect the camera pixel and the projector pixel as shown in Fig. 1. This model can be considered as an extension of the stereo vision model. Intrinsic and extrinsic parameters of the camera and the projector are determined by the system calibration. With known positions of the camera pixel and the projector pixel, the 3D coordinate of the object point can be calculated through triangulation.

Here, we choose several representative calibration models, which are the linear phase-height model, the inverse linear phase-height model, the polynomial phase-height model, the governing equation based phase-height model, and the triangular stereo model where the projector is calibrated without the assistance of a calibrated camera.

### 3.1. Classic phase-height models

In the early phase-height model [53], the optical axes of the projector and the camera are supposed to keep parallel. Both axes are perpendicular to a reference plane. Further, the distances of the projector and camera are the same from the reference plane. The illustration is shown in Fig. 2, where $h$ is the height of measured point $B$ and $d$ the distance from optical centers (i.e., $O_p$ and $O_c$) to the reference plane.

According to Fig. 2, since $\Delta DEB$ is similar to $\Delta O_c O_p B$, the height of point $B$ can be calculated by

$$h = \frac{\overline{DE}\cdot d}{l + \overline{DE}} \tag{4}$$

At the reference plane, uniform projected fringes can be observed as the axis of projector is perpendicular to the reference plane. Consequently, the length of $\overline{DE}$ can be obtained by $\overline{DE} = \frac{\phi_D - \phi_E}{2\pi} p = \frac{\phi_{DE}}{2\pi} p$, where $p$ is the width of a projected stripe on reference plane. Then, Eq. (4) can be written as

$$h = \frac{\phi_{DE}\cdot p\cdot d}{\phi_{DE}\cdot p + 2\pi l} \tag{5}$$

where $p$, $l$, $d$ are the parameters to be calibrated in this phase-height model. Usually, they can be measured manually once the system is fixed. As a result, the height is determined by the phase difference $\phi_{DE}$. From the viewpoint of the projector, the phase is invariant for points on the same light ray, leading to $\phi_B = \phi_E$. Then, the phase difference $\phi_{DE}$ can be solved as $\phi_{DE} = \phi_{DB}$, where $D$ is a point on the reference plane. As points $B$ and $D$ would be captured by the same camera pixel, we need to obtain two phase maps. First, only the phase of the reference plane is measured. Then, the object's phase is measured when it is deployed in front of the reference plane. By subtracting the reference plane's phase from the object's phase, the phase difference is obtained.

The parallel-axis classic model is intuitive and easy to understand. Nevertheless, it is difficult to apply since the geometric constraints are hard to meet in practical applications. Also, it is not easy to measure the parameters accurately by hand. Further, the parallel-axis arrangement tends to limit the common view of the projector and the camera, thus restricting the measurement volume.

Cross-axis phase-height models are developed by removing the assumption of parallel optical axes. We keep the distance $d$ unchanged and slightly rotate the camera or the projector as illustrated in Fig. 3. It can be seen that the stripe's width on the reference plane is constant if only the camera is rotated as shown in Fig. 3(a). In this case, since the coefficients $p$, $d$, and $l$ are constant, Eq. (5) is still applicable. If we rotate the projector to illuminate the object from the side (Fig. 3(b) and Fig. 3(c)), however, the distribution of fringes projected on the reference plane will no longer be uniform. Therefore, the phase-height relationship should be changed into

$$h = \frac{\phi_{DE}\cdot p(x)\cdot d}{\phi_{DE}\cdot p(x) + 2\pi l} \tag{6}$$

where the width of a projected stripe is changed from a constant $p$ into a variable $p(x)$ that is determined by the position on the reference plane.

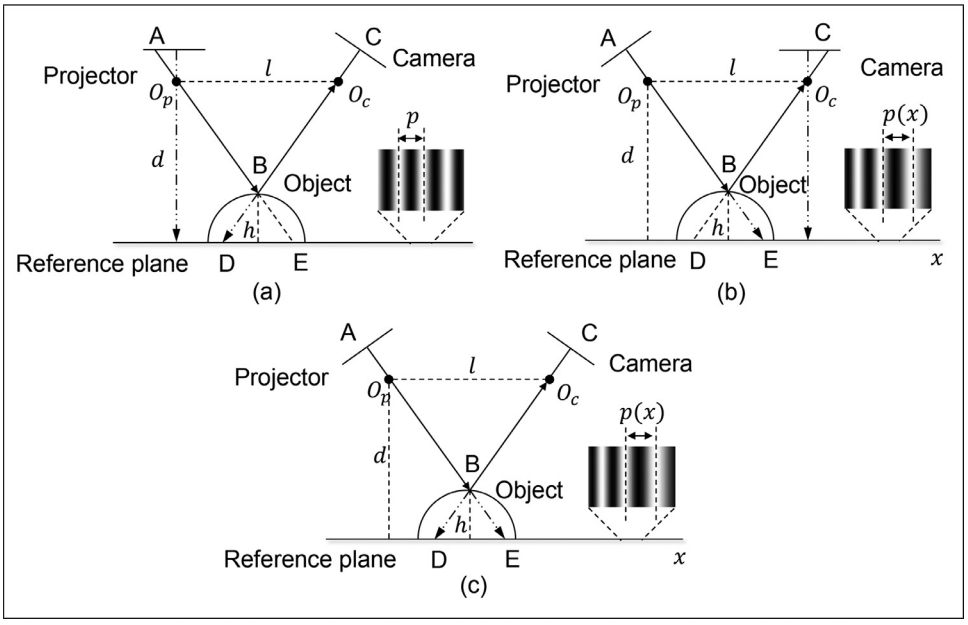


**Fig. 3.** Schematics of several classic phase-height models where the optical axes of the camera and the projector are not parallel. (a) The camera is tilted; (b) the projector is tilted; (c) both of the camera and the projector are tilted.

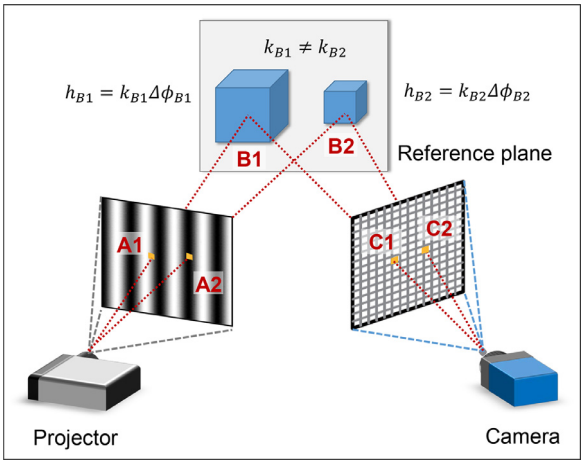


**Fig. 4.** Pixel-wise mapping of the linear phase-height model.

The varying fringe brings about a nonlinear spatial distribution of the carrier frequency [69,78,149]. To cope with this issue, one can derive the distribution of $p(x)$ explicitly [76] or pre-distort the projected fringe patterns [68,72].

### 3.2. Linear phase-height model

The linear phase-height model is the most simplest calibration model in fringe projection [79]. According to Fig. 2, if $l \gg \overline{DE}$ for some cases, Eq. (4) can be simplified as

$$h \approx \frac{\overline{DE} \cdot d}{l} = \frac{p \cdot d}{2\pi l}\phi_{DE} = k\phi_{DE} \tag{7}$$

where $k$ is the only parameter to be calibrated. It is noted that Eq. (7) is valid under the assumption that points $A$, $B$, $C$, $D$ and $E$ are in the same plane (i.e., the plane of the paper). In practice, however, the height of measured objects may not be uniform. Therefore, to measure the whole object, pixel-wise mapping is preferred, which is demonstrated in Fig. 4. Therefore, with $\Delta\phi(x, y)=\phi_{DE}(x, y)$, Eq. (7) is converted into

$$h(x, y) = k(x, y)\Delta\phi(x, y) \tag{8}$$

To calculate the pixel-wise parameter $k(x, y)$, we only need to measure a reference plane at a known height in theory. However, more measurements at different heights are suggested to increase the accuracy of the calibrated $k(x, y)$, which can be solved by applying the least-square algorithm. The advantage of the linear model is that it is simple and can be computed without a heavy computation burden. However, the disadvantage is the limited measurement accuracy when the assumption $l \gg \overline{DE}$ is not satisfied.

### 3.3. Linear inverse phase-height model

To release the strict geometric constraints, researchers developed a flexible model where there is no strict geometric constraint on the system configuration [95]. It is called the linear inverse phase-height model in this work, as there is a linear relationship between the reciprocal height and the reciprocal phase difference. In this model, the camera and the projector can be deployed arbitrarily as long as the measured object can be illuminated and captured by them. The phase-height relationship can be written as

$$\frac{1}{h(x, y)} = a(x, y) + b(x, y)\frac{1}{\Delta\phi(x, y)} \tag{9}$$

where $\Delta\phi(x, y)$ is the phase difference, $a(x, y)$ and $b(x, y)$ are pixel-wise parameters to be calibrated. A simulation of a fitted curve is shown in Fig. 5. By the least-square algorithm, a reference plane measured at several known heights can be used to fit parameters $a(x, y)$ and $b(x, y)$.

It is noteworthy that Eq. (9) can be rearranged into

$$\Delta\phi(x, y) = h(x, y)\Delta\phi(x, y)a(x, y)+h(x, y)b(x, y). \tag{10}$$

At first glance, both Eq. (9) and Eq. (10) are suitable for calibration. In fact, however, their performance is different. Due to the presence of noise in actual measurements, the reconstruction error of Eq. (9) shows a dependency on the objects height [82,150]. The higher the object, the larger the error. By comparison, Eq. (10) can estimate the height under the same condition more robustly. Our experiment in Section 4 will further demonstrate their different performance.

### 3.4. Polynomial phase-height model

By rearranging Eq. (9), we can also obtain

$$h(x, y) = \frac{\Delta\phi(x, y)}{a(x, y)\Delta\phi(x, y) + b(x, y)} \tag{11}$$

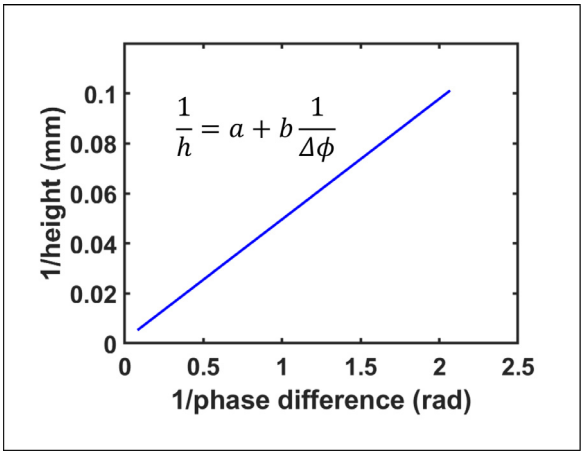


**Fig. 5.** The linear relationship between the reciprocal height and the reciprocal phase difference.

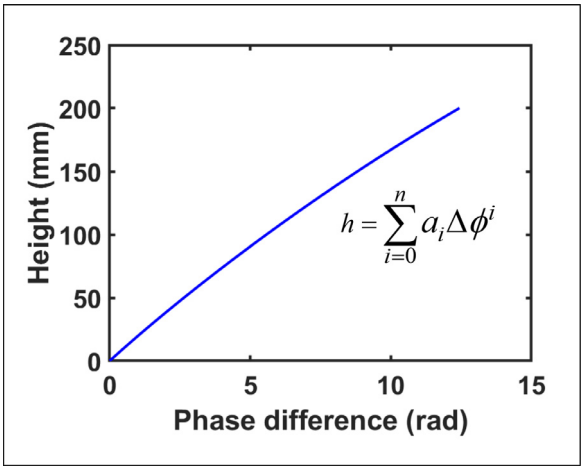


**Fig. 6.** A simulated polynomial fitting of the relationship between the height and the phase difference $\Delta\phi$.

This equation shows a nonlinear relationship between the height $h(x, y)$ and the phase difference $\Delta\phi(x, y)$ [82]. Thus, these parameters can be estimated with nonlinear least-square algorithms. However, the performance of the nonlinear fitting process depends on the initial values of $a(x, y)$ and $b(x, y)$, which may affect the stability of the algorithm. To cope with this issue, researchers suggested a polynomial fitting approach to approximate this nonlinear relationship [144], leading to

$$h(x, y) = \sum_{i=0}^{n} a_i(x, y)\Delta\phi(x, y)^i \tag{12}$$

where $a_i(x, y)$ is the pixel-wise coefficient to be calibrated. The coefficients are often saved after the calibration and then loaded during the 3D measurement. A simulated polynomial phase-height mapping is shown Fig. 6. Actually, the effect of lens distortion on the surface reconstruction can be relieved by increasing the degree of polynomial. However, $n$ should be carefully adjusted as Runge phenomenon may occur when a high-degree polynomial function is used [81].

### 3.5. Governing equation based phase-height model

The governing equation based phase-height model is also a generalized model where the projector and the camera can be arranged arbitrarily [84]. The phase-height mapping can be written as

$$h(x, y) = \frac{C_0 + C_1\phi(x, y) + \left[C_2 + C_3\phi(x, y)\right]x + \left[C_4 + C_5\phi(x, y)\right]y}{D_0 + D_1\phi(x, y) + \left[D_2 + D_3\phi(x, y)\right]x + \left[D_4 + D_5\phi(x, y)\right]y} \tag{13}$$

where $C_0$–$C_5$ and $D_0$–$D_5$ are coefficients that are calibrated using gauge blocks with known heights or reference planes with known heights. The coefficients can be estimated by nonlinear regression methods, e.g., the Levenberg-Marquardt algorithm. Unlike the models mentioned in Sections 3.1 to 3.4, the governing equation based phase-height model converts the object's phase $\phi$ rather than the phase difference $\Delta\phi$ into the height. The reason is that there is a one to one correspondence between the object's phase (i.e., the unwrapped phase) and the object's height for each pixel [33]. The second difference is that the pixel coordinate $(x, y)$ is involved during the height calculation as shown in Eq. (13). Therefore, instead of being pixel-wise, the coefficients $C_0$–$C_5$ and $D_0$–$D_5$ are constant for all of the pixels. This model can save the memory used to store the coefficients.

### 3.6. Triangular stereo model

In the mentioned phase-height models, neither the camera nor the projector is calibrated. However, the triangular stereo model requires the calibration of both the camera and the projector. The pine-hole model is often used to calibrate a camera. The projector can be treated as an inverse camera because the projection process is inverse to the imaging process. Therefore, the projector can be calibrated in the same way we calibrate the camera. The key to calibrate a projector is that it needs to capture feature points as a camera does. Therefore, the phase plays a significant role in correlating a camera pixel to a projector pixel. This model assumes that the projector and the camera are deployed arbitrarily as long as the measured object is in their common viewing field. In this section, we first introduce the camera calibration and then explain how to calibrate the projector. At last, the joint calibration of the camera and the projector is presented.

#### 3.6.1. Camera calibration

To calibrate a camera, the pin-hole model is widely used to describe the imaging process, which is illustrated in Fig. 7. $O_w - X_wY_wZ_w$ is the world coordinate system, and $O_c - X_cY_cZ_c$ is the camera coordinate system where $O_c$ is the projection center of the camera. The imaging plane is at $z_c = f$, where $f$ is the focal length. The imaging plane is parallel to the plane $X_cY_cO_c$. A virtual normalized plane is constructed at $z_c = 1$ and is parallel to the imaging plane. Assume that there is a point $\mathbf{X}=\left(x_w, y_w, z_w\right)^T$ in 3D space and it is captured by the pixel $\mathbf{x} = (x, y)^T$ at the imaging plane, where $T$ means transpose. In this paper, we represent their homogeneous coordinates as $\tilde{\mathbf{X}}=\left(x_w, y_w, z_w, 1\right)^T$ and $\tilde{\mathbf{x}} = (x, y, 1)^T$, respectively. The imaging process of a pin-hole model can be written as [151]

$$\alpha\tilde{\mathbf{x}} = \mathbf{K}[\mathbf{R}|\mathbf{t}]\tilde{\mathbf{X}} \tag{14}$$

where $\alpha$ is a scalar factor, $\mathbf{R}$ a $3\times3$ rotation matrix and $\mathbf{t}$ a $3\times1$ translation vector. The extrinsic matrix $[\mathbf{R}|\mathbf{t}]$ transforms the point $\tilde{\mathbf{X}}=\left(x_w, y_w, z_w, 1\right)^T$ into the camera coordinate system by

$$\tilde{\mathbf{X}}_c = \begin{bmatrix}\mathbf{R} & \mathbf{t}\\ 0 & 1\end{bmatrix}\tilde{\mathbf{X}} \tag{15}$$

The matrix $\mathbf{K}$ in Eq. (14) is the intrinsic matrix of the camera and can be written as

$$\mathbf{K} = \begin{pmatrix} f_x & s & x_0\\ 0 & f_y & y_0\\ 0 & 0 & 1\end{pmatrix} \tag{16}$$

where $f_x=f/\Delta x$ and $f_y=f/\Delta y$ are focal lengths (with the unit in pixels) after considering the size of camera pixels, in which $\Delta x$ and $\Delta y$ are the size of the pixel at different directions. They would be different if the camera pixel is not in a square shape. $(x_0, y_0)^T$ is the principal point that is near the center of the imaging plane. $s$ is the skew coefficient which is not zero if the image axes are not perpendicular.

The pin-hole model represented by Eq. (14) describes a linear imaging process. In practice, however, the imaging process is nonlinear due

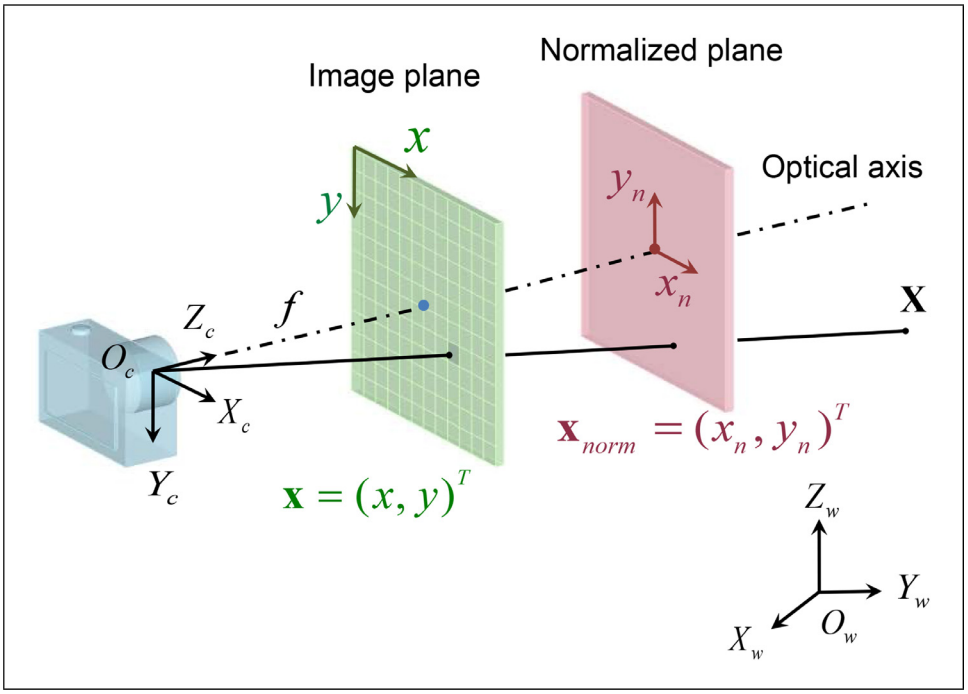


**Fig. 7.** Diagram of a pinhole camera.

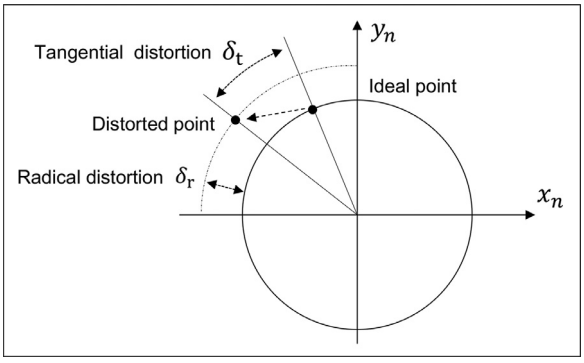


**Fig. 8.** The effects of the radical distortion and the tangential distortion.

to the presence of lens distortion that can change the direction of incoming light. Ideally, the projection of $\mathbf{X}_c=(x_c, y_c, z_c)^T$ at the normalized plane is

$$\begin{pmatrix} x_n \\ y_n \end{pmatrix} = \begin{pmatrix} x_c/z_c \\ y_c/z_c \end{pmatrix} \tag{17}$$

The lens distortion changes the position of $\mathbf{x}_{norm} = (x_n, y_n)^T$, thus affecting the imaging process. In this paper, we introduce two kinds of lens distortion that are the radical distortion and the tangential distortion, whose effects are shown in Fig. 8. The calibration of these kinds of lens distortion can meet the requirement of most cases. The radical distortion $\boldsymbol{\delta}_\mathbf{r}$ can be written as [152]

$$\boldsymbol{\delta}_\mathbf{r} = \begin{pmatrix} k_1 r_n^2 + k_2 r_n^4 + k_3 r_n^6 \\ k_1 r_n^2 + k_2 r_n^4 + k_3 r_n^6 \end{pmatrix} \begin{pmatrix} x_n \\ y_n \end{pmatrix} \tag{18}$$

where $r_n = \sqrt{x_n^2 + y_n^2}$. The tangential distortion $\boldsymbol{\delta}_\mathbf{t}$ can be expressed as [153]

$$\boldsymbol{\delta}_\mathbf{t} = \begin{pmatrix} 2k_4 x_n y_n + k_5(2x_n^2 + r_n^2) \\ k_4(2y_n^2 + r_n^2) + 2k_5 x_n y_n \end{pmatrix}. \tag{19}$$

In Eqs. (18) and (19), a vector $\mathbf{k}= (k_1, k_2, k_3, k_4, k_5)$ can be used to represent the coefficients of the lens distortion, in which $(k_1, k_2, k_3)$ are the coefficients of the radical distortion and $(k_4, k_5)$ are those of the tangential distortion. Affected by the lens distortion, the normalized point can be represented as

$$\mathbf{x}_{dn} = \begin{pmatrix} x_{dn} \\ y_{dn} \end{pmatrix} = \begin{pmatrix} x_n \\ y_n \end{pmatrix} + \delta_r + \delta_t \tag{20}$$

The final imaging pixel is changed into $\mathbf{x}_d = (x_d, y_d)^T$ by

$$\tilde{\mathbf{x}}_d = \mathbf{K}\tilde{\mathbf{x}}_{dn} \tag{21}$$

The goal of camera calibration is to estimate the intrinsic matrix K, the extrinsic matrix $[\mathbf{R}|\mathbf{t}]$, and the distortion vector $\mathbf{k}$. Given $n$ images of a calibration board and $m$ feature points found on the calibration board. These coefficients can be obtained by minimizing the sum of reprojection errors

$$\min_{\arg} \sum_{i=1}^{n} \sum_{j=1}^{m} \left\| \mathbf{x}_{ij} - \hat{\mathbf{x}}_{ij}(\boldsymbol{\theta}_\mathbf{K}, \boldsymbol{\theta}_i^\mathbf{RT}) \right\|^2 \tag{22}$$

where $\boldsymbol{\theta}_\mathbf{K}$ consists of entries in the intrinsic matrix K and the distortion vector $\mathbf{k}$. $\boldsymbol{\theta}_i^\mathbf{RT}$ consists of coefficients in extrinsic matrix $[\mathbf{R}_i|\mathbf{t}_i]$. $\mathbf{x}_{ij}$ is the actual image coordinate extracted by image processing techniques and $\hat{\mathbf{x}}_{ij}(\theta_K, \theta_i^{RT})$ is the projection of point $\mathbf{X}_j$ in image $i$ according to Eq. (14) where the lens distortion of Eqs. (18) and (19) are considered. To solve Eq. (22), a nonlinear least-square fitting algorithm can be used, e.g., the Levenberg-Marquardt algorithm. Nowadays, there are some toolboxes available for the camera calibration, which are easy to use and very helpful [154–156]. For more details on the camera calibration, readers may refer to Refs. [151,157].

### 3.6.2. Projector calibration

To calibrate a projector, the strategy without the assistance of a calibrated camera is introduced [102,103,119]. The key to the projector calibration is to find the feature points seen by the projector. As the fringe projection system consists of a camera and a projector, the camera can help the projector see the feature points. The phase information can be used to find the projector pixel, which corresponds to a camera pixel with the same phase.

Analogous to the camera calibration, the projector calibration requires to capture a calibration board at some random positions. The calibration board is placed in front of the fringe projection system. Then, the

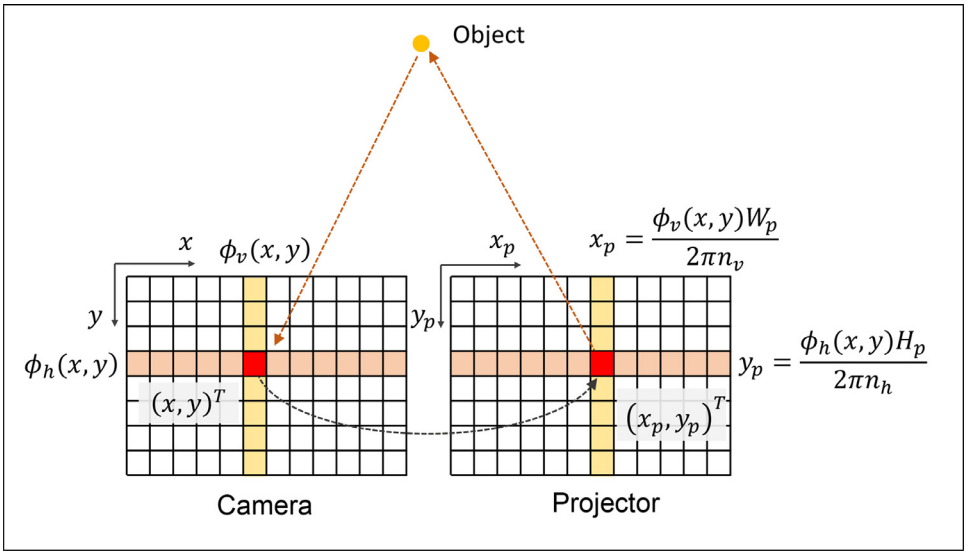


**Fig. 9.** Schematic of how a projector *sees* a measured point with the assistance of an uncalibrated camera.

projector illuminates the calibration board with fringe images, e.g., two sets of $N$-step phase-shifting images, where one set consists of vertical fringes and the other consists of horizontal fringes. An image of uniform illumination can be obtained by averaging either set of the $N$ fringe images. The diagram of how a projector sees a measured point is shown in Fig. 9. Assume that a feature point on the calibration board is captured by a camera pixel $(x, y)^T$. We can calculate an absolute phase map $\phi_v(x, y)$ with the vertical fringe patterns by the $N$-step phase-shifting algorithm and temporal phase unwrapping algorithms. If the resolution of the projector is $H_p \times W_p$, and the number of stripes of the projected pattern is $n_v$, the camera pixel $(x, y)^T$ would correspond to a vertical line on the projector plane with the coordinate of

$$x_p = \frac{\phi_v(x, y)W_p}{2\pi n_v}. \tag{23}$$

By using the absolute phase extracted from the horizontal phase-shifting images, we can find a horizontal line on the projector plane with the coordinate of

$$y_p = \frac{\phi_h(x, y)H_p}{2\pi n_h}. \tag{24}$$

where $\phi_h(x, y)$ is the absolute phase calculated with the horizontal fringe images and $n_h$ the number of horizontal stripes of projected fringes. By using Eqs. (23) and (24), the feature point is seen by the projector pixel $(x_p, y_p)^T$ which is the intersection of the vertical and the horizontal line. Given $n$ images of a calibration board and $m$ points found on the calibration board, we can calibrate the projector in a similar way we calibrate the camera

$$\min_{\arg} \sum_{i=1}^{n}\sum_{j=1}^{m} \left\| \mathbf{x}_{ij}^{p} - \hat{\mathbf{x}}_{ij}^{p}(\boldsymbol{\theta}_{\mathbf{K}}^{p}, \boldsymbol{\theta}_{i}^{\mathbf{R}^p\mathbf{T}^p}) \right\|^2 \tag{25}$$

where $\boldsymbol{\theta}_{\mathbf{K}}^{p}$ consists of the coefficients in the projectors intrinsic matrix and distortion vector. $\boldsymbol{\theta}_{i}^{\mathbf{R}^p\mathbf{T}^p}$ consists of coefficients of the extrinsic matrix $[\mathbf{R}_i^{\mathbf{p}}|\mathbf{t}_i^{\mathbf{p}}]$ of the projector. $\mathbf{x}_{ij}^{p}$ is obtained by Eqs. (23) and (24), and $\hat{\mathbf{x}}_{ij}^{p}$ is the projection of point $\mathbf{X}_j$ in image $i$.

### 3.6.3. Camera-projector joint calibration

The purpose of joint calibration is to improve the calibration accuracy through minimizing the reprojection errors of the camera and the projector simultaneously. Prior to the joint calibration, the camera and the projector are calibrated separately by the same set of calibration images, which ensures the same world coordinate system. Assume a point $\mathbf{X} = (x_w, y_w, z_w)^T$ is captured by the camera pixel $\mathbf{x}=(x, y)^T$ and by the projector pixel $\mathbf{x}^p=(x_p, y_p)^T$, respectively, the joint calibration can be carried out by

$$\min_{\arg} \sum_{i=1}^{n}\sum_{j=1}^{m} \left\| \mathbf{x}_{ij} - \hat{\mathbf{x}}_{ij}(\boldsymbol{\theta}_{\mathbf{K}}^{\mathbf{c}}, \boldsymbol{\theta}_{i}^{\mathbf{RT}}) \right\|^2 + \left\| \mathbf{x}_{ij}^{p} - \hat{\mathbf{x}}_{ij}^{p}(\boldsymbol{\theta}_{\mathbf{K}}^{\mathbf{p}}, \boldsymbol{\theta}^{\mathbf{pc}}) \right\|^2 \tag{26}$$

where $\boldsymbol{\theta}_{\mathbf{K}}^{\mathbf{c}}$, $\boldsymbol{\theta}_{\mathbf{K}}^{\mathbf{p}}$, $\boldsymbol{\theta}_{i}^{\mathbf{RT}}$ and $\boldsymbol{\theta}^{\mathbf{pc}}$ include all the coefficients to be calibrated. $\boldsymbol{\theta}^{\mathbf{pc}}$ consists of a rotation matrix $\mathbf{R}^{\mathbf{pc}}$ and a translation matrix $\mathbf{t}^{\mathbf{pc}}$, which can convert a point in the projector coordinate system to the one in the camera coordinate system through $(x_c, y_c, z_c)^T = \mathbf{R}^{\mathbf{pc}}(x_p, y_p, z_p)^T + \mathbf{t}^{\mathbf{pc}}$. Equation (26) can be solved by nonlinear fitting algorithms (e.g., the Levenberg-Marquardt algorithm), where the initial values can be obtained from the results of the separate calibration of the camera and the projector.

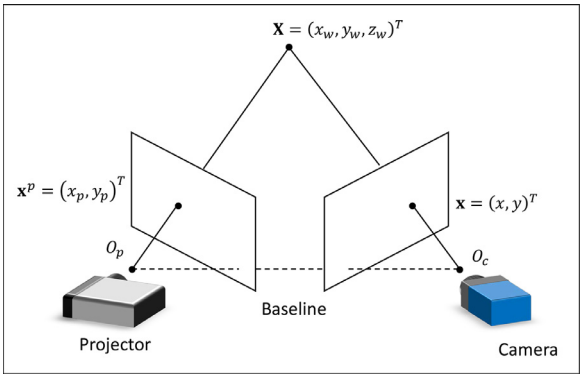


**Fig. 10.** Schematic of the 3D reconstruction in the triangular stereo model.

### 3.6.4. 3D reconstruction

When the camera and the projector have been calibrated, we can simply use stereo vision algorithms to reconstruct 3D models [17]. Assume we have a 3D point $\mathbf{X}=(x_w, y_w, z_w)^T$ to be reconstructed. As shown in Fig. 10, this point is captured by the camera pixel $\mathbf{x}=(x, y)^T$ and the projector pixel $\mathbf{x}^p=(x_p, y_p)^T$, which is calculated by Eqs. (23) and (24). When the lens distortion has been corrected, we can reconstruct the 3D point $\mathbf{X}$ by

$$\tilde{\mathbf{x}} = \mathbf{P}^c\tilde{\mathbf{X}} \tag{27}$$

$$\tilde{\mathbf{x}}^p = \mathbf{P}^p\tilde{\mathbf{X}} \tag{28}$$

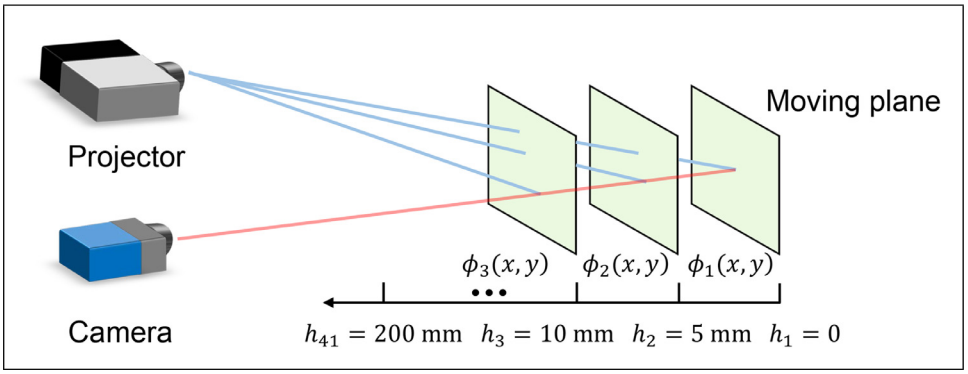


**Fig. 11.** The process to calibrate the measurement volume for the phase-height models.

where $\mathbf{P}^c$=$\mathbf{K}[\mathbf{R}|\mathbf{t}]$ and $\mathbf{P}^p$=$\mathbf{K}^p[\mathbf{R}^p|\mathbf{t}^p]$ are the projection matrix of the camera and the projector, respectively. Equations (27) and (28) can be rearranged into $\mathbf{A}\tilde{\mathbf{X}} = 0$, where $\mathbf{A}$ is

$$\mathbf{A} = \begin{pmatrix} x\mathbf{P}_c^3 - \mathbf{P}_c^1 \\ y\mathbf{P}_c^3 - \mathbf{P}_c^2 \\ x_p\mathbf{P}_p^3 - \mathbf{P}_p^1 \\ y_p\mathbf{P}_p^3 - \mathbf{P}_p^2 \end{pmatrix} \tag{29}$$

where $\mathbf{P}_c^i$ is the $i$th row of $\mathbf{P}^c$ and $\mathbf{P}_p^i$ the $i$th row of $\mathbf{P}^p$. The solution to Eq. (29) is the null space of $\mathbf{A}$. As Eq. (29) is redundant actually, we can reduce the number of projected fringe image by only projecting a single set of fringe images in the 3D reconstruction [105]. Assume that the projector and camera are arranged horizontally and only vertical fringe images are projected, we can obtain the horizontal coordinate $x_p$ by using the phase $\phi_v(x, y)$ according to Eq. (23). If the camera projection matrix $\mathbf{P}^c$ is

$$P^c = \begin{pmatrix} p_{11}^c & p_{12}^c & p_{13}^c & p_{14}^c \\ p_{21}^c & p_{22}^c & p_{23}^c & p_{24}^c \\ p_{31}^c & p_{32}^c & p_{33}^c & p_{34}^c \end{pmatrix} \tag{30}$$

And the projector projection matrix $\mathbf{P}^p$ is

$$P^p = \begin{pmatrix} p_{11}^p & p_{12}^p & p_{13}^p & p_{14}^p \\ p_{21}^p & p_{22}^p & p_{23}^p & p_{24}^p \\ p_{31}^p & p_{32}^p & p_{33}^p & p_{34}^p \end{pmatrix} \tag{31}$$

Given the camera pixel $\mathbf{x}$=$(x, y)^T$ and the projector horizontal coordinate $x_p$, the 3D coordinate can be calculated by

$$\begin{pmatrix} x_w \\ y_w \\ z_w \end{pmatrix} = \begin{pmatrix} p_{11}^c - p_{31}^c x & p_{12}^c - p_{32}^c x & p_{13}^c - p_{33}^c x \\ p_{21}^c - p_{31}^c y & p_{22}^c - p_{32}^c y & p_{23}^c - p_{33}^c y \\ p_{21}^p - p_{31}^p x_p & p_{22}^p - p_{32}^p x_p & p_{23}^c - p_{33}^c x_p \end{pmatrix}^{-1} \begin{pmatrix} p_{14}^c - p_{34}^c x \\ p_{24}^c - p_{34}^c y \\ p_{24}^c - p_{34}^c x_p \end{pmatrix} \tag{32}$$

## 4. Experiments

To test the performace of the calibration approaches, we built a fringe projection system. It contains a camera (acA640-750um, Basler) and a projector (DLP LightCrafter 4500, Texas Instruments). They were deployed horizontally on an optical table without strict geometric constraints. The focal length of the camera lens (Computar) is 8 mm. In our experiments, we compared the linear phase-height model, the linear inverse phase-height model, the polynomial phase-height model, the governing equation based phase-height model, and the triangular stereo model through both quantitative and qualitative evaluations. For the qualitative experiment, sample codes (in Matlab) for the calibration and the 3D reconstruction of these models are provided.

To calculate the phase, we projected three sets of 12-step phase-shifting patterns. In the three sets of images, the spatial frequencies of projected patterns are 1, 8, 64, respectively. The 12-step phase-shifting algorithm was used to obtain the wrapped phase maps, and the multi-frequency temporal unwrapping method was applied for absolute phase unwrapping [62]. In the 3D reconstructions, the unwrapped phase extracted from the fringe images with the highest frequency (i.e., 64) was converted into height maps and 3D coordinates.

### 4.1. Quantitative experiments

In quantitative experiments, the measurement volume to be calibrated was located 1 m to 1.2 m in front of the fringe projection system. First, we implemented the phase-height calibration models. We adopted a white marble slab as the reference plane, which was moved by a motorized linear positioner stage (PI, M-521 of positioning accuracy 0.1 $\mu m$). The illustration is shown in Fig. 11. The height of $h = 0$ mm was set at 1.2 m in front of the system. During the calibration, the marble slab moved at a step of 5 mm toward the system from $h = 0$ mm and stoped at $h = 200$ mm. At each position, three sets of phase-shifting patterns were projected and captured. Once the phase was obtained, the phase-height mapping was calibrated by the linear phase-height model, the linear inverse phase-height model, the polynomial phase-height model, and the governing equation based phase-height model.

To calibrate the system with the triangular stereo model, we used a flat calibration target that is a black mental board painted with white dots, as shown in Fig. 12. These dots are arranged in 9 rows and 11 columns. The diameter of the big dot is 15 mm and that of the small dot is 7.5 mm. The distance of each center is 25 mm. The calibration board was deployed randomly within the same range from $h = 0$ mm to $h = 200$ mm. We projected three sets of vertical and horizontal 12-step

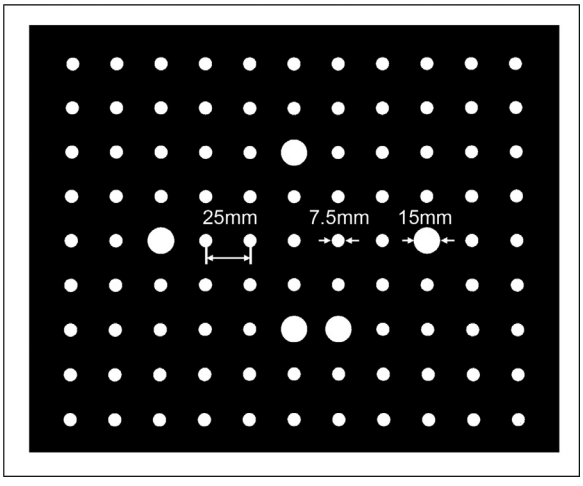


**Fig. 12.** The calibration board used in the calibration of the triangular stereo model.

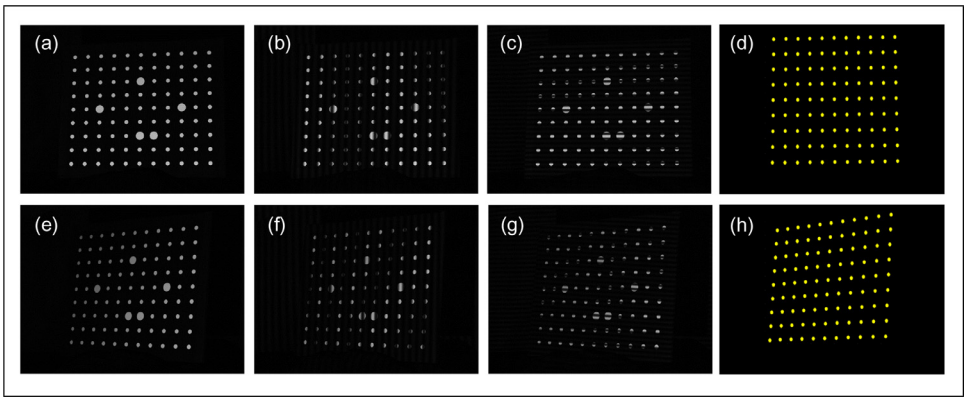


**Fig. 13.** Experimental results of the calibration board at two different positions. (a) and (e) show the image of the calibration board at two different positions, respectively; (b) and (f) are the captured vertical fringe images; (c) and (g) are the captured horizontal fringe images; (d) and (h) are the calculated centers for the projector calibration.

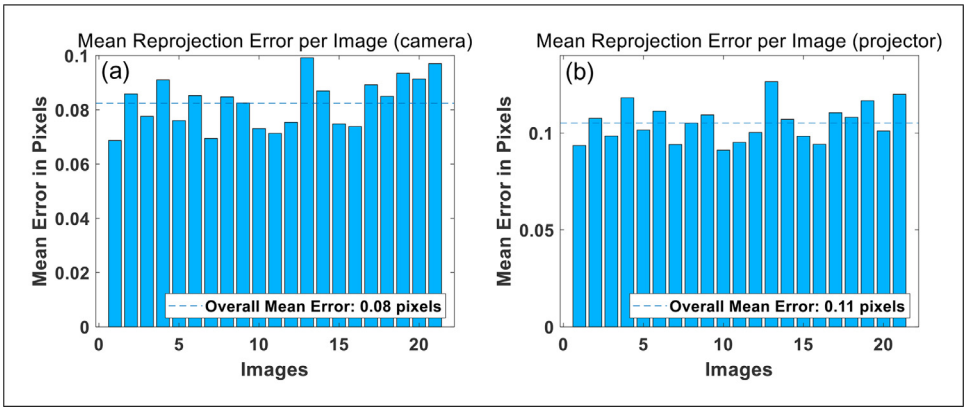


**Fig. 14.** The reprojection errors of the camera (a) and the projector (b).

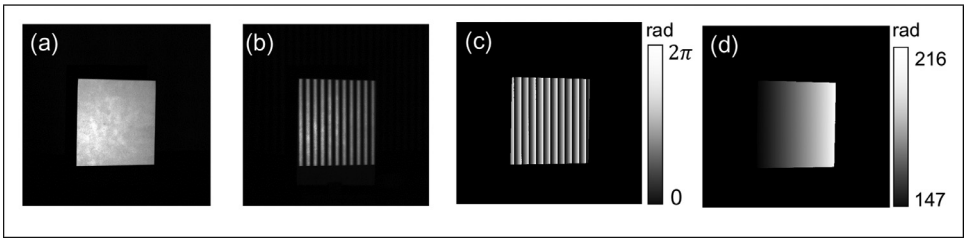


**Fig. 15.** The white marble slab measured at $h = 0$ mm. (a) The image of the marble slab; (b) one of the captured fringe images; (c) the wrapped phase; (d) the unwrapped phase.

phase-shifting patterns on the calibration board at each position and captured 21 different positions in total. After calculating the average of captured 12-step phase-shifting images at each position, we obtained 21 images of the calibration board. Fig. 13 shows the images of the calibration board captured at two different positions. The 2D coordinates and the phase of circles' centers were calculated for the calibration of the camera and the projector. The calibration errors of the camera and the projector are shown in Fig. 14, where the overall mean reprojection errors of the camera and the projector are 0.08 pixels and 0.11 pixels, respectively. In the 3D reconstruction, the world coordinate system was set on the calibration board at the first position. Only vertical phase-shifting images were used for 3D measurements.

*4.1.1. Calibration of the full measurement volume*

In the first quantitative experiment, we calibrated and tested the selected models within the full range that is between $h = 0$ mm and $h = 200$ mm. The marble slab moving with 10 mm as a step, i.e., $h = 0$ mm, $h = 10$ mm, $h = 20$ mm to $h = 200$ mm, was used to fit the phase-height models. In the polynomial model, a fifth-order function was applied. Fig. 15 shows experimental results of the marble slab at $h = 0$ mm. In the triangular stereo model, images of the calibration board captured at 21 different positions were used to calculate the intrinsic and the extrinsic parameters of the camera and the projector. Moreover, the nonlinear triangular stereo model with the correction of the lens distortion was implemented.

To test the performance of each approach, the white marble slab was measured at different positions, i.e., $h = 5$ mm, $h = 15$ mm, $h = 25$ mm to $h = 195$, which were accurately controlled by the positioner stage. We compared the estimated height with its nominal value. The mean absolute error (MAE) and the standard deviation (STD) of the whole measured surface were calculated for quantitative evaluations. The measurement errors of the selected calibration methods are shown in Figs. 16. The MAE of the linear phase-height model shows significant errors of a shape of 'W' as can be seen in Figs. 16(a). Large errors appeared when the object was measured at $h = 0$, $h = 100$, and $h = 200$. The reason is that the actual relationship between the phase difference and the height is not linear. The line fitted by the linear phase-height model has two intersections with the curve obtained from the real phase-height relationship. Therefore, the MAE is small when the object's position is near the intersection. For the rest positions, however, the MAE tends to increase. From Figs. 16(d), the STD of the linear model is also relatively large. In the linear inverse phase-height model, the phase-height mapping was calibrated by Eq. (9) (denoted by Inverse (1)) and Eq. (10) (denoted by Inverse (2)), respectively. In Figs. 16(a) and (b), the MAE and the STD

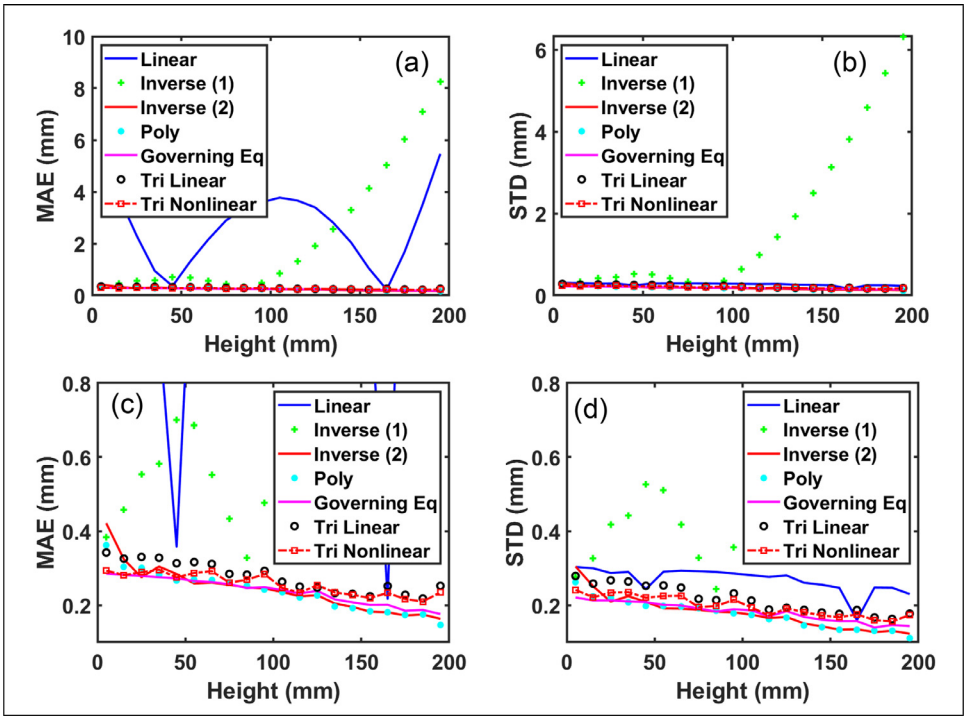


**Fig. 16.** Measurement errors at different heights. (a) The mean absolute error (MAE); (b) the standard deviation (STD); (c) zoom-in view of (a); (d) zoom-in view of (b).

of Inverse (1) are very obvious. The errors are relatively small between $h = 0$ mm and $h = 100$ mm but start to soar once the object height is larger than 100 mm. Thus, the MAE and the STD of Inverse (1) are dependent on the object height. By comparison, the MAE and the STD of Inverse (2) are much smaller as demonstrated in Figs. 16(c) and (d). In the following experiments, the linear inverse phase-height mapping was implemented by Eq. (10).

As to the triangular stereo models, the nonlinear triangular model shows reduced MAE and STD due to the correction of the lens distortion of the camera and the projector. Compared with the triangular stereo models, the governing equation based phase-height model demonstrates smaller errors. The polynomial phase-height model and the linear inverse phase-height model (Inverse 2) have the smallest MAE and STD among all of the models. We find that the errors of the linear inverse phase-height model, the polynomial phase-height model, the governing equation based phase-height model, and the triangular stereo model decrease when the object's height is increasing. The reason is that the higher the object, the closer it is to the fringe projection system. As the baseline between the camera and the projector is fixed, the system is more sensitive to the varying height when the object moves towards it.

*4.1.2. Calibration of half of the measurement volume*

Measured objects are usually arranged within a volume that has been fully calibrated. In this experiment, we only calibrated the measurement range between $h = 0$ mm and $h = 100$ mm. But, we still tested the measurement accuracy of each calibration approach in the full measurement range, which are at $h = 5$ mm, $h = 15$ mm,..., $h = 185$ mm, and $h = 195$ mm. Namely, the heights of $h = 105$ mm to $h = 195$ mm were not swept with our calibration target. This experiment aims to investigate the sensitivity of calibration methods to 3D reconstructions of objects that exceed the valid calibrated volume.

In Figs. 17(a) and (b), we can see that the polynomial phase-height model shows the greatest dependence on the calibration space. In the calibrated volume $h = 0$ mm to $h = 100$ mm, the MAE and the STD are small, as shown in Figs. 17(c) and (d). However, the errors raised very rapidly once the object was outside the calibrated space. It can be seen that the MAE and STD of the linear phase-height model, the linear inverse phase-height model, and the governing equation based phase-height model also increased when the calibration space failed to cover the object. However, they are not as obvious as the errors of the polynomial phase-height model. The triangular stereo models are observed with the smallest sensitivity to the calibration volume among the selected calibration models. In the uncalibrated range of $h = 100$ mm to $h = 200$ mm, their MAE and STD are smaller than 0.5 mm and 0.3 mm respectively. It is noteworthy that they are still larger than the errors when the full range has been calibrated, as shown in Figs. 16(c) and (d). From this experiment, we can see that we should make the calibration space cover the entire object as much as possible for better surface reconstruction with higher accuracy. If not, triangular stereo models may be better choices for the system calibration.

*4.1.3. Calibration with different phase-shifting algorithms*

The phase computation is essential to the calibration of system coefficients and the 3D reconstruction. The purpose of this experiment is to study the influence of different phase-shifting algorithms. To this end, we compared the performance of the 3-step, 4-step, 6-step, and 12-step phase-shifting algorithms. In the implementation of each selection model, the same phase-shifting algorithm was used in the coefficient calibration and the 3D reconstruction.

For the linear phase-height model, according to Fig. 18(a) different phase-shifting algorithms show almost the same distribution of the MAE, which is very large and is dependant on the object height. From Fig. 18(d), its STD reduces when the number of steps increases. As shown in Figs. 18(b), (c), (e), and (f), and Figs. 19(a) and (d), the influence of different phase-shifting algorithms on calibrating approaches of the linear inverse phase-height model, the polynomial phase-height model, and the governing equation based phase-height model are similar. Their calibration accuracy can be improved with phase-shifting algorithms of a large number of steps. As to the triangular stereo models, the 4-step phase-shifting method performed slightly better than the 3-step phase-shifting method when the object's height is smaller than 50 mm. The difference is tiny for the rest positions. The MAE and the STD of the triangular stereo models decrease significantly when the number of steps increases to 6 and 12, as shown in Figs. 19(b), (c), (e) and (f). Through comparisons, the nonlinear triangular stereo model shows higher measurement accuracy than the linear one as the former corrected the effect

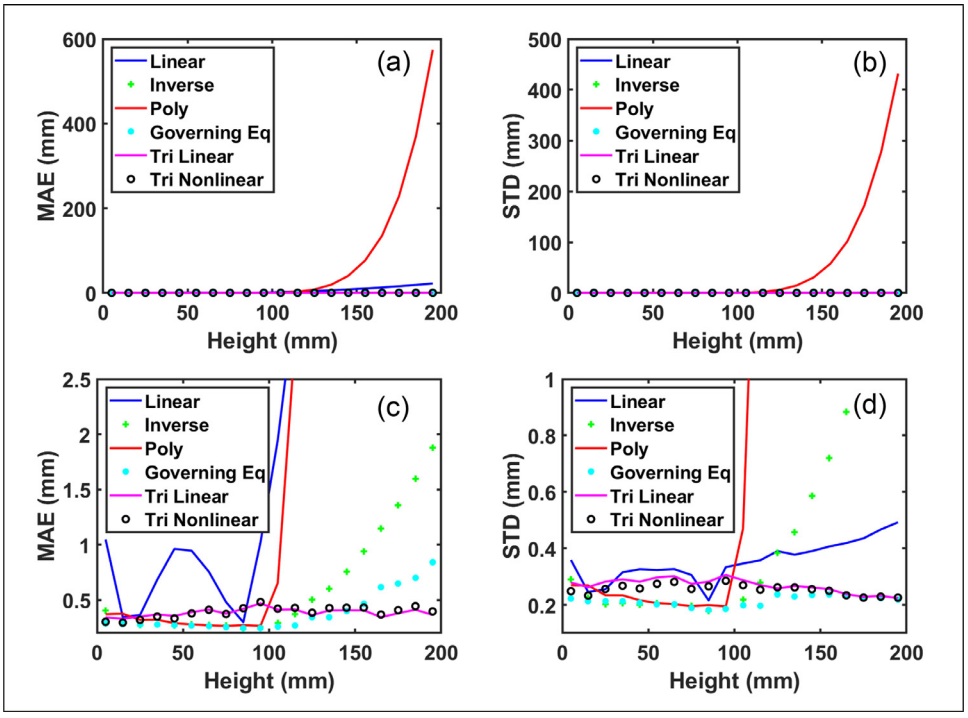


**Fig. 17.** The measurement error at different heights when only half of the volume was calibrated. (a) The mean absolute error (MAE); (b) the standard deviation (STD); (c) zoom-in view of (a); (d) zoom-in view of (b).

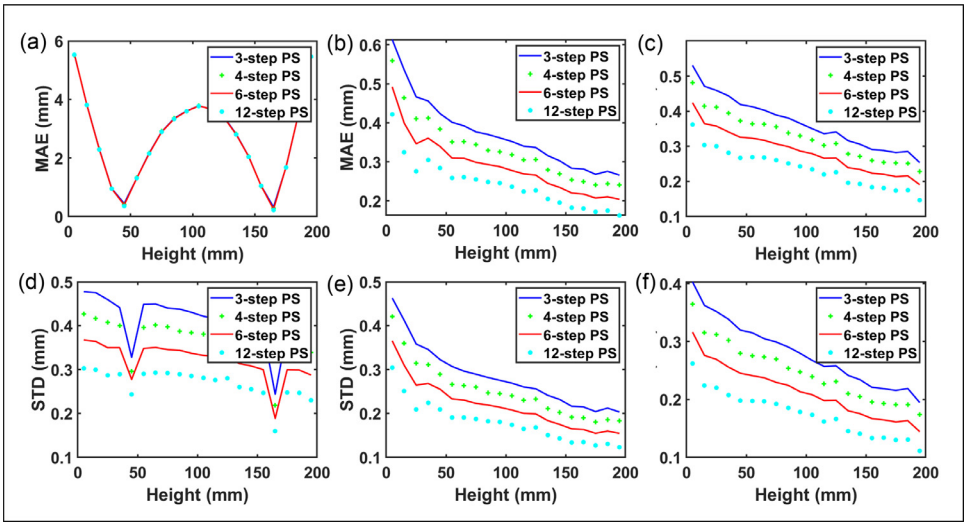


**Fig. 18.** The measurement error at different heights by different phase-shifting algorithms (part 1). (a) MAE of the linear phase-height model; (b) MAE of the linear inverse phase-height model; (c) MAE of the polynomial phase-height model; (d) STD of the linear phase-height model; (e) STD of the linear inverse phase-height model; (f) STD of the polynomial phase-height model.

of lens distortion. In summary, phase-shifting algorithms with a large number of steps are favorable for improving the performance of the system calibration.

### 4.2. Qualitative experiment

In the qualitative experiment, we slightly changed the measurement volume that was between 600 mm to 700 mm in front of the system. For the calibration of the phase-height models, the reference plane with $h = 0$ mm was set at a distance of 700 mm. The range calibrated was 100 mm. The moving step of the marble slab is 5 mm. In the polynomial phase-height model, a third degree polynomial was applied. For the triangular stereo models, the calibration board was measured with 20 different positions within this range.

The measurement object is a plaster model that was placed within the calibrated volume. The 12-step phase-shifting algorithm was applied in the coefficient calibration and 3D reconstruction. Fig. 20 shows the estimated surface of each model, where the color represents the height of each point. Overall, the test object has been measured successfully with all of the selected methods. We further investigated a cross-section at row 280 of the estimated height maps. The results are demonstrated in Fig. 21, where the zoomed-in area corresponds to a section of the object's face. As the real digital 3D model used in manufacturing is not available for this purchased object, we used an industrial 3D scanner (OKIO 3M with an accuracy of 0.025mm) to obtain a reference profile. We find that although the reconstructed plaster looks good with the linear phase-height model as shown in Fig. 20(a), its actual profile deviates from the reference surface as can be seen in Fig. 21. For the linear triangular stereo model, its error is smaller than that of the linear phase-height model but is still larger than those of the rest models. For

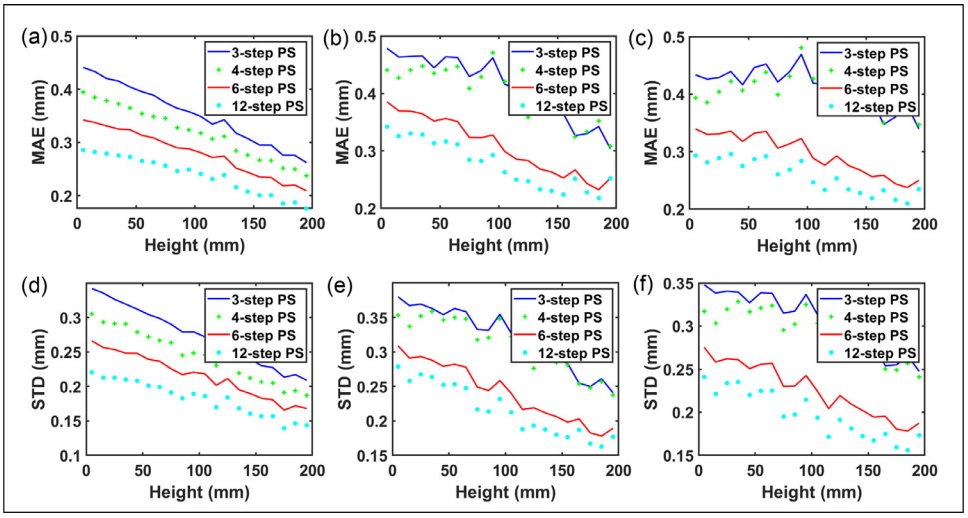


**Fig. 19.** The measurement error at different heights by different phase-shifting algorithms (part 2). (a) MAE of the governing equation based phase-height model; (b) MAE of the triangular stereo model without lens distortion corrected; (c) MAE of the triangular stereo model with lens distortion corrected; (d) STD of the governing equation based phase-height model; (e) STD of the triangular stereo model without lens distortion corrected; (f) STD of the triangular stereo model with lens distortion corrected.

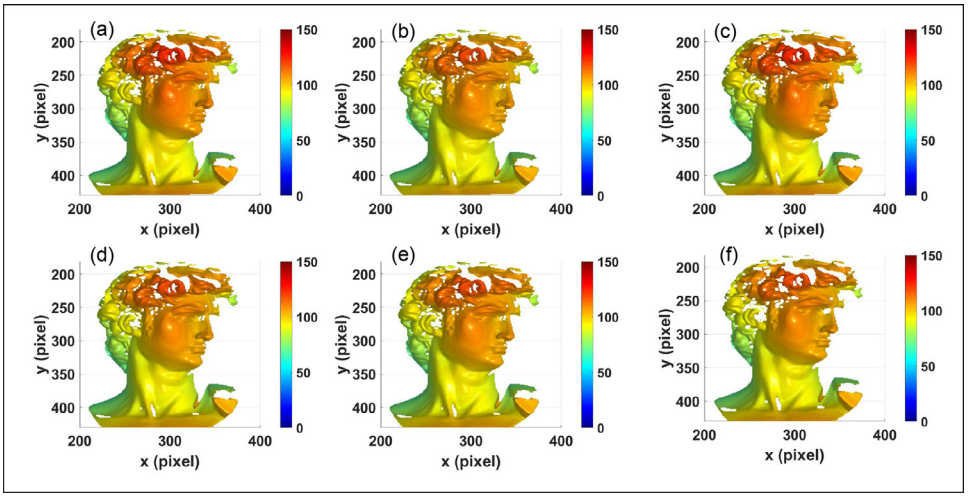


**Fig. 20.** Height maps of the test plaster by different calibration methods. (a) The linear phase-height model; (b) the linear inverse phase-height model; (c) the polynomial phase-height model; (d) the governing equation based phase-height model; (e) the triangular stereo model without lens distortion corrected; (f) the triangular stereo model with lens distortion corrected.

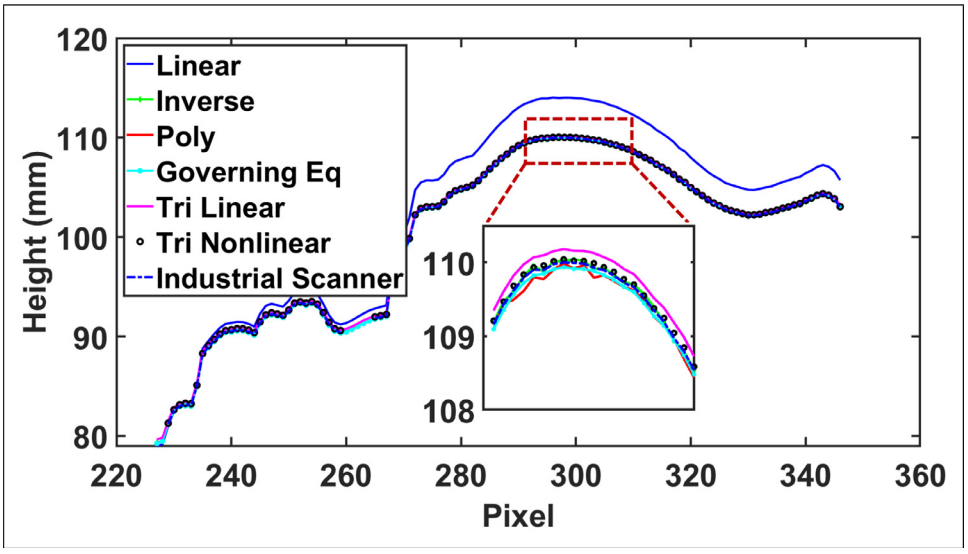


**Fig. 21.** Comparison of the cross section of the measured height for different calibration method.

| | Height or 3D coordinates | Extraction of feature points | Effect of lens distortion | Effect of the nonlinearity of system | Calibration out of the lab | Valid volume | Real-time 3D measurements | Reduction of the cost |
|---|---|---|---|---|---|---|---|---|
| Linear | Height | Points on a flat plane at different known heights | Sensitive | Sensitive, prior correction or use a linear projector | Moderate | Moderate | GPU, LUTs, multi-threading | Replace the positioner stage with a calibrated camera |
| Linear inverse | Height | Same as above | Sensitive, increase the degree of the fitting function | Same as above | Moderate | Moderate | Same as above | Same as above |
| Polynomial | Height | Same as above | Same as above | Same as above | Moderate | Moderate | Same as above | Same as above |
| Governing equation | Height | Same as above or points on several gauge blocks | Same as above | Same as above | Moderate | Moderate | Same as above | Same as above |
| Triangular | 3D coordinates | Corners, centers or other feature points on calibration boards | Sensitive, explicit distortion correction | Same as above or develop a stereo fringe projection system | Good | Large | Same as above | Budget calibration tools + feature points correction or bundle adjustment |

**Fig. 22.** Discussion and comparative assessment of the representative calibration methods from different aspects.

the polynomial phase-height model, the reconstructed area is not very smooth as tiny grainy errors can be observed. Among all of the methods, the nonlinear triangular stereo model, the linear inverse phase-height model, and the governing equation based phase-height model performed 3D reconstructions that are more close to the reference 3D result.

## 5. Discussion

In this section, we further discuss the selected calibration methods from eight aspects. We aim to facilitate the practical implementation of these techniques and help users choose an appropriate calibration algorithm under given practical conditions. The comparison is summarized in Fig. 22.

### 5.1. Estimation of heights or 3D coordinates

The phase-height models are developed to calculate the height according to the phase. But, the relationship between the phase and the horizontal coordinates $x$ and $y$ is often not considered. References [77,83,85,88,92,137–140,145,158,159] introduced several improved phase-height models that can convert the phase into $x$ and $y$ coordinates. By contrast, the triangular stereo model can estimate $x$, $y$, and $z$ coordinate inherently since the projector has been treated as an inverse camera. Two rays back-projecting from the camera pixel and the projector pixel can intersect at a 3D point in the measurement space.

### 5.2. Extraction of feature points

For phase-height models, the feature points are the points that are used for fitting the phase-height function. To accurately extract the phase information from each point, one needs to deploy a flat board on the positioner stage carefully. It is important to make sure that the board's normal direction is parallel to its moving direction. For the triangular stereo model, the positions of feature points on the calibration board should be measured accurately. The calibration board is usually made by painting specific patterns, e.g., circular patterns or checkboard patterns. When a checkboard target is applied, the corner is often used as the feature point. However, the phase at the corner may be inaccurate when a black and white (B/W) checkboard is measured by a B/W camera. In this case, a red-blue checkboard is a better choice than the B/W checkboard [102]. By comparison, when a black calibration board with white dot patterns is used, the circles' centers are treated as feature points. The phase of the centers can be measured accurately with a B/W camera, as the white circles can be measured with fringe images of a favorable signal-to-noise ratio. However, it is noteworthy that a circle may be imaged as an ellipse under a perspective projection. Therefore, the ellipses center may not be the real center of the circle. Compensation to the position of the extracted center is beneficial to improve the calibration accuracy [114].

### 5.3. Elimination of the lens distortion

The lens distortion changes the shape of both projected and imaged fringe patterns, thus decreasing the accuracy of 3D reconstructions. The effect of the lens distortion may be trivial if high accuracy 3D measurement is not required. For precise 3D measurements, however, we are supposed to take it into account. For the linear inverse model, the polynomial model, and the governing equation based model, one can reduce the influence of the lens distortion by increasing the degree of the fitting function [82,93,142]. In contrast, the lens distortion of the camera and the projector is often calibrated explicitly in the triangular stereo model. Thus, the compensation of the lens distortion is more intuitive in triangular stereo models [110,112].

### 5.4. Effect of the nonlinearity of fringe projection systems

The nonlinear response (i.e., the gamma distortion) of the fringe projection system changes the shape of captured sinusoidal fringe images. It affects the accuracy of both system calibration and 3D reconstruction. When a commercial projector is in use, one may test the system's nonlinearity before system calibration. In our experiments, the influence of the nonlinearity is very small as the projector and the camera are manufactured without a preset gamma. For both the phase-height models and the triangular stereo model discussed above, the gamma correction should be applied if the effect of gamma is not trivial [40–44]. It is noteworthy that there is a variant of the triangular stereo model that is robust to the gamma distortion induced by the projector [160]. The system involves two cameras and a projector. The 3D reconstruction is obtained by matching the corresponding points of the two cameras with the same phase. Therefore, as long as the phase of these two pixels is the same, regardless of its accuracy, they can still be used for accurate 3D reconstruction.

### 5.5. System calibration out of the lab

A calibration apparatus or target can provide dimensional information of the real world. For the phase-height models, a flat board with a high-precision positioner stage or several gauge blocks are required to provide prior knowledge of height. For the triangular stereo model, the calibration target can be a board painted with pre-designed 2D patterns or a 3D target with feature points distributed in the 3D space. For the calibration out of labs, the triangular stereo model is more favorable since

the calibration target can be deployed arbitrarily in the measurement volume. To some extent, the usage of the positioner stage increases the complexity of the calibration process. To make the phase-height calibration more flexible, one may perform the phase-height mapping assisted by a calibrated camera [141,142,144,145].

### 5.6. Valid calibration and measurement volumes

Our experiments show that the 3D reconstruction is more accurate if the calibration target can cover the whole measurement range in the system calibration. For the compared calibration methods, they have different valid/ideal volumes for 3D reconstruction. For the phase-height models that use a positioner stage, the valid calibrated volume tends to be limited within the area swept by the moving plane. In contrast, the calibration board can be placed freely in the measurement range in the triangular stereo model. As the measuring volume can be better covered, the triangular stereo model is more appropriate for inspections of large objects.

### 5.7. Applications for real-time 3D measurements

Real-time 3D measurement is a hot topic in fringe projection profilometry. Compared with traditional strategies for measuring static scenes, it can provide 3D videos of dynamic scenes [33,52,56,63,161–164]. For real-time inspections, the key is to increase the measuring speed for the 3D reconstruction. For both the phase-height and the triangular stereo models, calibrated parameters can be saved to the computers disk in advance. Real-time phase computation, phase unwrapping, and phase-height/phase-3D reconstructions are then performed by parallel processing technologies such as Graphics Processing Unit (GPU), look-up tables, and multi-threading techniques [105,137,161].

### 5.8. Reduction of the cost

The accuracy of calibration tools determines that of the system. However, high-precision calibration tools such as the positioner stage and the calibration board are expensive, which can even account for more than 50% of the total cost. To reduce the cost, the phase-height models may be implemented by a calibrated camera [141,142,144,145], which can save the cost of a positioner stage. For the triangular stereo model, a budget calibration target can be made by printing calibration patterns on a piece of paper and then adhering it to a flat surface. In this case, as the self-made calibration boards precision is not high enough, the photogrammetry can be used to rectify the position of the feature point on the calibration board in advance [106,165]. Alternatively, the bundle adjustment algorithm [110,119] may be involved in the system calibration, as it considers the influence of inaccurate feature points in the estimation of system coefficients.

## 6. Conclusion

System calibration is significant to fringe projection profilometry. In this paper, we have compared several commonly used calibration methods in fringe projection. The selected models are the linear phase-height model, the linear inverse phase-height model, the polynomial phase-height model, the governing equation based phase-height model, and the triangular stereo model. We have implemented both quantitative and qualitative experiments. In the quantitative evaluation, a planar object has been tested at several known heights. The experimental results show that the measurement error of the linear phase-height model relies on the height of the measured object. It is hard for this method to obtain high-accuracy 3D reconstructions. When the measurement volume has been calibrated completely, the linear inverse model and the polynomial model performed better than other methods. When the measurement volume is not calibrated fully or the test object is so large that it is out of the calibrated range, the triangular stereo model shows the best performance among the selected models.

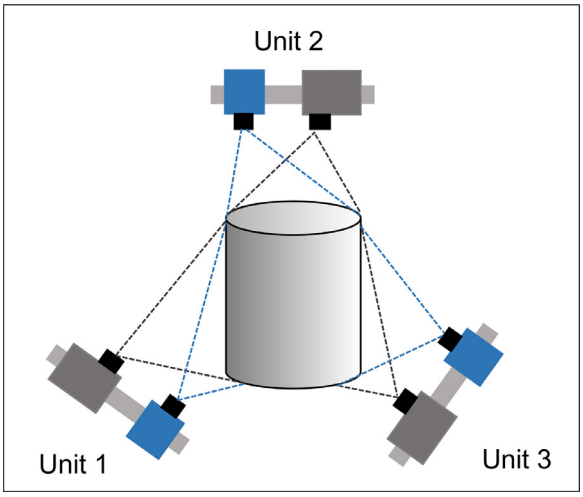


**Fig. 23.** Diagram of a network that includes some measuring units for different areas.

We have also investigated the effect of phase accuracy on the system calibration by calculating the phase with different phase-shifting algorithms. For all of the compared calibrated models, experimental results show that the larger the number of the phase shifts the higher the reconstruction accuracy. For the triangular stereo model, the performance of the 3-step phase-shifting algorithm and the 4-step phase-shifting algorithm is similar. Its accuracy can be improved obviously when the number of phase shifts increases to 6 and 12. In the qualitative experiment, a complex plaster model has been tested. Compared with the reference 3D model obtained with a high-accuracy industrial 3D scanner, 3D reconstructions of the linear inverse model, the governing equation based model, and the nonlinear triangular stereo model have demonstrated higher quality than those of the rest models. To better understand these calibration methods, we have further discussed them from eight aspects. We hope that the comparative review would be useful to choose an appropriate calibration algorithm for various applications.

Several issues are beyond the scope of this work but are still noteworthy in practical applications:

**(1) 3D measurement network for large objects**. Fringe projection is developed for 3D surface measurements. Therefore, only illuminated areas can be reconstructed. For large objects, stitching algorithms, like the iterative closest point (ICP), are often used to merge entire 3D point clouds from some 3D segments. However, errors tend to accumulate in the merging process, which can cause a severe mismatch between the first and the last point clouds. To cope with this issue, one may build a measuring network consisting of several independent 3D units as shown in Fig. 23. As each unit is responsible for a particular area, the complete 3D result can be obtained by fusing separate 3D pieces together. The calibration of such a network is more complex than that of a single unit, since all of the units should be considered into a global system. The calibration targets with 3D feature points are recommended for calibrating such networks, as it is easy for the units at a different position to find appropriate feature points [166,167].

**(2) Fast calibration for in-situ applications**. For industrial and in-situ applications, the environment is full of disturbing factors. For example, the vibration of measuring systems during the transportation can cause changes to the extrinsic parameters of the system but keep the intrinsic matrix almost unchanged. Therefore, a fast calibration would be useful to improve the efficiency of in-situ 3D measurements. Schreiber *et al.* reported a self-calibration method to calibrate the system during each measurement, which can remove the effect of vibrations [119]. Zhao *et al.* introduced a fast re-calibration method for extrinsic parameters correction when the relative position is changed [168].

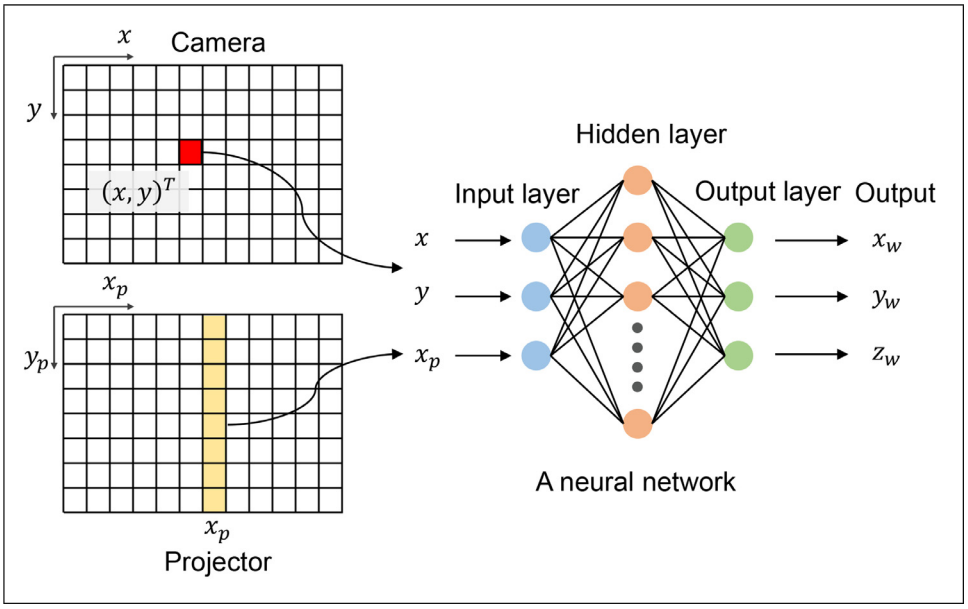


**Fig. 24.** Illustration of 3D reconstruction using a neural network.

**(3) System calibration with deep learning**. Nowadays deep learning techniques are widely applied to computer vision [169–171] and computational optical imaging [172–175]. In the fringe projection, researchers have demonstrated that the performance of phase measurement [51], phase unwrapping [64,65], and fringe pattern denoising [176] can be improved with the assistance of deep learning techniques. Deep learning is a subset of the machine learning, which has been proved to be useful to the calibration of fringe projection systems years ago [177–179]. An illustration is shown in Fig. 24. With the inputs of the camera coordinates and one of the projector coordinates, the 3D coordinate can be computed by a trained neural network. The advantage is that the lens distortion can be handled implicitly by the neural network. However, it is inconvenient for users to obtain training data, as one has to move a calibration board step by step with a precise positioner stage. The performance of the neural network would be further improved with recent developments of the deep neural network. Recently, the correction of the lens distortion of projector using deep learning has been reported [180]. We believe advanced deep learning techniques will demonstrate promising potentials to the system calibration in the future.

## Funding

This work was supported by National Natural Science Foundation of China (61722506, 61705105), National Key R&D Program of China (2017YFF0106403), Leading Technology of Jiangsu Basic Research Plan (BK20192003), Final Assembly “13th Five-Year Plan” Advanced Research Project of China (30102070102), Equipment Advanced Research Fund of China (61404150202), The Key Research and Development Program of Jiangsu Province (BE2017162), Outstanding Youth Foundation of Jiangsu Province (BK20170034), National Defense Science and Technology Foundation of China (2019-JCJQ-JJ-381), “333 Engineering” Research Project of Jiangsu Province (BRA2016407), Fundamental Research Funds for the Central Universities (30920032101,30919011222,30917011204,30916011322).

## Declaration of Competing Interest

The authors declare that they have no known competing financial interests or personal relationships that could have appeared to influence the work reported in this paper.

## References

[1] Harding K. The advent of three-dimensional optical metrology has brought many benefits to industrial quality control of aircraft engines, according to the turbine-blade manufacturer GE.. Nat Photonics 2008;2:4.
[2] Malamas EN, Petrakis EG, Zervakis M, Petit L, Legat J-D. A survey on industrial vision systems, applications and tools. Image Vis Comput 2003;21(2):171–88.
[3] Land WS, Zhang B, Ziegert J, Davies A. In-situ metrology system for laser powder bed fusion additive process. Procedia Manuf 2015;1:393–403.
[4] Xing HZ, Zhang QB, Braithwaite CH, Pan B, Zhao J. High-speed photography and digital optical measurement techniques for geomaterials: fundamentals and applications. Rock Mech Rock Eng 2017;50(6):1611–59.
[5] Ford KR, Myer GD, Hewett TE. Reliability of landing 3D motion analysis: implications for longitudinal analyses. Medicine & Science in Sports & Exercise 2007;39(11):2021–8.
[6] Pan B, Qian K, Xie H, Asundi A. Two-dimensional digital image correlation for in-plane displacement and strain measurement: a review. Meas Sci Technol 2009;20(6):062001.
[7] Qian J, Feng S, Tao T, Hu Y, Liu K, Wu S, et al. High-resolution real-time 3D model reconstruction of a handheld object with fringe projection profilometry. Opt Lett 2019;44(23):5751.
[8] Song K, Hu S, Wen X, Yan Y. Fast 3D shape measurement using fourier transform profilometry without phase unwrapping. Opt Lasers Eng 2016;84:74–81.
[9] Geng J. Structured-light 3D surface imaging: a tutorial. Adv Opt Photonics 2011;3(2):128.
[10] Brown GM. Overview of three-dimensional shape measurement using optical methods. Opt Eng 2000;39(1):10.
[11] Xiong Z, Zhang Y, Wu F, Zeng W. Computational depth sensing : toward high-performance commodity depth cameras. IEEE Signal Process Mag 2017;34(3):55–68.
[12] Chen C, Gao N, Wang X, Zhang Z, Gao F, Jiang X. Generic exponential fringe model for alleviating phase error in phase measuring profilometry. Opt Lasers Eng 2018;110:179–85.
[13] Huang L, Idir M, Zuo C, Asundi A. Review of phase measuring deflectometry. Opt Lasers Eng 2018;107:247–57.
[14] Peng K, Cao Y, Wu Y, Xiao Y. A new pixel matching method using the modulation of shadow areas in online 3D measurement. Opt Lasers Eng 2013;51(9):1078–84.
[15] Vermeulen MMPA, Rosielle P, Schellekens P. Design of a high-precision 3d-coordinate measuring machine. CIRP Ann 1998;47(1):447–50.
[16] Cui Y, Schuon S, Chan D, Thrun S, Theobalt C. 3D shape scanning with a time-of-flight camera. In: 2010 IEEE computer society conference on computer vision and pattern recognition. San Francisco, CA, USA: IEEE; 2010. p. 1173–80.
[17] Scharstein D, Szeliski R, Zabih R. A taxonomy and evaluation of dense two-frame stereo correspondence algorithms. In: Proceedings IEEE workshop on stereo and multi-baseline vision (SMBV 2001). Kauai, HI, USA: IEEE Comput. Soc; 2001. p. 131–40. ISBN 978-0-7695-1327-0.
[18] Zhang Q, Su X. High-speed optical measurement for the drumhead vibration. Opt Express 2005;13(8):3110–16.
[19] Zuo C, Chen Q, Feng S, Feng F, Gu G, Sui X. Optimized pulse width modulation pattern strategy for three-dimensional profilometry with projector defocusing. Appl Opt 2012;51(19):4477.
[20] Cai Z, Liu X, Peng X, Gao BZ. Ray calibration and phase mapping for structured–light-field 3D reconstruction. Opt Express 2018;26(6):7598.

[21] Feng S, Chen Q, Zuo C, Li R, Shen G, Feng F. Automatic identification and removal of outliers for high-speed fringe projection profilometry. Opt Eng 2013;52(1):013605.
[22] Qian J, Feng S, Li Y, Tao T, Han J, Chen Q, et al. Single-shot absolute 3D shape measurement with deep-learning-based color fringe projection profilometry. Opt Lett 2020;45(7):1842.
[23] Wang Y, Zhang S. Superfast multifrequency phase-shifting technique with optimal pulse width modulation. Opt Express 2011;19(6):5149.
[24] Feng S, Zuo C, Yin W, Gu G, Chen Q. Micro deep learning profilometry for high--speed 3D surface imaging. Opt Lasers Eng 2019;121:416–27.
[25] Zuo C, Tao T, Feng S, Huang L, Asundi A, Chen Q. Micro fourier transform profilometry (FTP): 3D shape measurement at 10,000 frames per second. Opt Lasers Eng 2018;102:70–91.
[26] Lei S, Zhang S. Flexible 3-D shape measurement using projector defocusing. Opt Lett 2009;34(20):3080.
[27] Zuo C, Chen Q, Gu G, Feng S, Feng F, Li R, et al. High-speed three-dimensional shape measurement for dynamic scenes using bi-frequency tripolar pulse-width–modulation fringe projection. Opt Lasers Eng 2013;51(8):953–60.
[28] Cai Z, Liu X, Peng X, Yin Y, Li A, Wu J, et al. Structured light field 3d imaging. Opt Express 2016;24(18):20324–34.
[29] Hyun J-S, Chiu GT-C, Zhang S. High-speed and high-accuracy 3D surface measurement using a mechanical projector. Opt Express 2018;26(2):1474.
[30] Zhang M, Chen Q, Tao T, Feng S, Hu Y, Li H, et al. Robust and efficient multi-frequency temporal phase unwrapping: optimal fringe frequency and pattern sequence selection. Opt Express 2017;25(17):20381.
[31] Wu Z, Zuo C, Guo W, Tao T, Zhang Q. High-speed three-dimensional shape measurement based on cyclic complementary gray-code light. Opt Express 2019;27(2):1283–97.
[32] Xu Y, Ekstrand L, Dai J, Zhang S. Phase error compensation for three-dimensional shape measurement with projector defocusing. Appl Opt 2011;50(17):2572.
[33] Feng S, Chen Q, Zuo C. Graphics processing unit assisted real-time three-dimensional measurement using speckle-embedded fringe. Appl Opt 2015;54(22):6865.
[34] Yin W, Feng S, Tao T, Huang L, Trusiak M, Chen Q, et al. High-speed 3D shape measurement using the optimized composite fringe patterns and stereo-assisted structured light system. Opt Express 2019;27(3):2411.
[35] Gonzalez-Jorge H, Rodríguez-Gonzálvez P, Martínez-Sánchez J, González-Aguilera D, Arias P, Gesto M, et al. Metrological comparison between Kinect I and Kinect II sensors. Measurement 2015;70:21–6.
[36] Heist S, Zhang C, Reichwald K, Kühmstedt P, Notni G, Tünnermann A. 5D hyperspectral imaging: fast and accurate measurement of surface shape and spectral characteristics using structured light. Opt Express 2018;26(18):23366.
[37] Heist S, Lutzke P, Schmidt I, Dietrich P, Kühmstedt P, Tünnermann A, et al. High--speed three-dimensional shape measurement using GOBO projection. Opt Lasers Eng 2016;87:90–6.
[38] Li Zhang, Curless B, Seitz S. Rapid shape acquisition using color structured light and multi-pass dynamic programming. IEEE Comput. Soc; 2002. p. 24–36. ISBN 978-0-7695-1521-2.
[39] Morano R, Ozturk C, Conn R, Dubin S, Zietz S, Nissano J. Structured light using pseudorandom codes. IEEE Trans Pattern Anal Mach Intell 1998;20(3):322–7.
[40] Guo H, He H, Chen M. Gamma correction for digital fringe projection profilometry. Appl Opt 2004;43(14):2906.
[41] Hoang T, Pan B, Nguyen D, Wang Z. Generic gamma correction for accuracy enhancement in fringe-projection profilometry. Opt Lett 2010;35(12):1992.
[42] Pan B, Kemao Q, Huang L, Asundi A. Phase error analysis and compensation for nonsinusoidal waveforms in phase-shifting digital fringe projection profilometry. Opt Lett 2009;34(4):416.
[43] Ma S, Quan C, Zhu R, Chen L, Li B, Tay C. A fast and accurate gamma correction based on Fourier spectrum analysis for digital fringe projection profilometry. Opt Commun 2012;285(5):533–8.
[44] Lei Z, Wang C, Zhou C. Multi-frequency inverse-phase fringe projection profilometry for nonlinear phase error compensation. Opt Lasers Eng 2015;66:249–57.
[45] Feng S, Zhang L, Zuo C, Tao T, Chen Q, Gu G. High dynamic range 3D measurements with fringe projection profilometry: a review. Meas Sci Technol 2018;29(12):122001.
[46] Jiang H, Zhao H, Li X. High dynamic range fringe acquisition: a novel 3-D scanning technique for high-reflective surfaces. Opt Lasers Eng 2012;50(10):1484–93.
[47] Feng S, Zhang Y, Chen Q, Zuo C, Li R, Shen G. General solution for high dynamic range three-dimensional shape measurement using the fringe projection technique. Opt Lasers Eng 2014;59:56–71.
[48] Zhang S, Yau S-T. High dynamic range scanning technique. Opt Eng 2009;48(3):033604.
[49] Zhang L, Chen Q, Zuo C, Feng S. High-speed high dynamic range 3D shape measurement based on deep learning. Opt Lasers Eng 2020;134:106245.
[50] Li D, Kofman J. Adaptive fringe-pattern projection for image saturation avoidance in 3D surface-shape measurement. Opt Express 2014;22(8):9887.
[51] Feng S, Chen Q, Gu G, Tao T, Zhang L, Hu Y, et al. Fringe pattern analysis using deep learning. Advanced Photonics 2019;1(02):1.
[52] Zuo C, Feng S, Huang L, Tao T, Yin W, Chen Q. Phase shifting algorithms for fringe projection profilometry: a review. Opt Lasers Eng 2018;109:23–59.
[53] Takeda M, Mutoh K. Fourier transform profilometry for the automatic measurement of 3-d object shapes. Appl Opt 1983;22(24):3977.
[54] Feng S, Zuo C, Tao T, Hu Y, Zhang M, Chen Q, et al. Robust dynamic 3-d measurements with motion-compensated phase-shifting profilometry. Opt Lasers Eng 2018;103:127–38.
[55] Su X, Zhang Q. Dynamic 3-d shape measurement method: a review. Opt Lasers Eng 2010;48(2):191–204.
[56] Qian J, Tao T, Feng S, Chen Q, Zuo C. Motion-artifact-free dynamic 3D shape measurement with hybrid Fourier-transform phase-shifting profilometry. Opt Express 2019;27(3):2713.
[57] Huang L, Kemao Q, Pan B, Asundi AK. Comparison of Fourier transform, windowed Fourier transform, and wavelet transform methods for phase extraction from a single fringe pattern in fringe projection profilometry. Opt Lasers Eng 2010;48(2):141–8.
[58] Zhong J, Weng J. Spatial carrier-fringe pattern analysis by means of wavelet transform: wavelet transform profilometry. Appl Opt 2004;43(26):4993–8.
[59] Kemao Q. Two-dimensional windowed Fourier transform for fringe pattern analysis: principles, applications and implementations. Opt Lasers Eng 2007;45(2):304–17.
[60] Li B, Liu Z, Zhang S. Motion-induced error reduction by combining Fourier transform profilometry with phase-shifting profilometry. Opt Express 2016;24(20):23289.
[61] Lu L, Xi J, Yu Y, Guo Q. New approach to improve the accuracy of 3-D shape measurement of moving object using phase shifting profilometry. Opt Express 2013;21(25):30610.
[62] Zuo C, Huang L, Zhang M, Chen Q, Asundi A. Temporal phase unwrapping algorithms for fringe projection profilometry: a comparative review. Opt Lasers Eng 2016;85:84–103.
[63] Tao T, Chen Q, Da J, Feng S, Hu Y, Zuo C. Real-time 3-d shape measurement with composite phase-shifting fringes and multi-view system. Opt Express 2016;24(18):20253.
[64] Yin W, Chen Q, Feng S, Tao T, Huang L, Trusiak M, et al. Temporal phase unwrapping using deep learning. Sci Rep 2019;9(1):20175.
[65] Qian J, Feng S, Tao T, Hu Y, Li Y, Chen Q, et al. Deep-learning-enabled geometric constraints and phase unwrapping for single-shot absolute 3D shape measurement. APL Photonics 2020;5(4):046105.
[66] Zheng D, Da F. Phase coding method for absolute phase retrieval with a large number of codewords. Opt Express 2012;20(22):24139.
[67] Li Z, Zhong K, Li YF, Zhou X, Shi Y. Multiview phase shifting: a full-resolution and high-speed 3D measurement framework for arbitrary shape dynamic objects. Opt Lett 2013;38(9):1389–91.
[68] Zhang Z, Towers CE, Towers DP. Uneven fringe projection for efficient calibration in high-resolution 3D shape metrology. Appl Opt 2007;46(24):6113.
[69] Zhang Q, Wu Z. A carrier removal method in Fourier transform profilometry with zernike polynomials. Opt Lasers Eng 2013;51(3):253–60.
[70] Sansoni G, Carocci M, Rodella R. Calibration and performance evaluation of a 3-Dimaging sensor based on the projection of structured light. IEEE Trans Instrum Meas 2000;49(3):628–36.
[71] Li W, Su X, Liu Z. Large-scale three-dimensional object measurement: a practical coordinate mapping and image data-patching method. Appl Opt 2001;40(20):3326.
[72] Fu Y, Luo Q. Fringe projection profilometry based on a novel phase shift method. Opt Express 2011;19(22):21739.
[73] Ortiz MH, Patterson EA. Location and shape measurement using a portable fringe projection system. Exp Mech 2005;45(3):197–204.
[74] Guo W, Wu Z, Xu R, Zhang Q, Fujigaki M. A fast reconstruction method for three-dimensional shape measurement using dual-frequency grating projection and phase–to-height lookup table. Optics & Laser Technology 2019;112:269–77.
[75] Xiao Y, Cao Y, Wu Y. Improved algorithm for phase-to-height mapping in phase measuring profilometry. Appl Opt 2012;51(8):1149.
[76] Wang Z, Du H, Bi H. Out-of-plane shape determination in generalized fringe projection profilometry. Opt Express 2006;14(25):12122.
[77] Yu C, Peng Q. A unified-calibration method in FTP-based 3D data acquisition for reverse engineering. Opt Lasers Eng 2007;45(3):396–404.
[78] Feng S, Chen Q, Zuo C, Sun J, Tao T, Hu Y. A carrier removal technique for fourier transform profilometry based on principal component analysis. Opt Lasers Eng 2015;74:80–6.
[79] Zhang S. High-resolution, real-time 3-D shape measurement. Citeseer; 2005. PhD Thesis.
[80] Asundi A, Wensen Z. Unified calibration technique and its applications in optical triangular profilometry. Appl Opt 1999;38(16):3556.
[81] Guo H. Least-squares calibration method for fringe projection profilometry. Opt Eng 2005;44(3):033603.
[82] Huang L, Chua PSK, Asundi A. Least-squares calibration method for fringe projection profilometry considering camera lens distortion. Appl Opt 2010;49(9):1539.
[83] Liu H, Su W-H, Reichard K, Yin S. Calibration-based phase-shifting projected fringe profilometry for accurate absolute 3D surface profile measurement. Opt Commun 2003;216(1–3):65–80.
[84] Du H, Wang Z. Three-dimensional shape measurement with an arbitrarily arranged fringe projection profilometry system. Opt Lett 2007;32(16):2438.
[85] Anchini R, Di Leo G, Liguori C, Paolillo A. A new calibration procedure for 3-d shape measurement system based on phase-shifting projected fringe profilometry. IEEE Trans Instrum Meas 2009;58(5):1291–8.
[86] Lv S, Jiang M, Su C, Zhang L, Zhang F, Sui Q, et al. Flexible calibration method of an FPP system based on a geometrical model and NLSM with fewer parameters. Appl Opt 2019;58(5):A7.
[87] Fu Y, Wang Y, Wang W, Wu J. Least-squares calibration method for fringe projection profilometry with some practical considerations. Optik (Stuttg) 2013;124(19):4041–5.
[88] Léandry I, Bréque C, Valle V. Calibration of a structured-light projection system: development to large dimension objects. Opt Lasers Eng 2012;50(3):373–9.
[89] Lu J, Mo R, Sun H, Chang Z. Flexible calibration of phase-to-height conversion in fringe projection profilometry. Appl Opt 2016;55(23):6381.

[90] Mao X, Chen W, Su X. Improved Fourier-transform profilometry. Appl Opt 2007;46(5):664.
[91] Su W-H, Liu H. Calibration-based two-frequency projected fringe profilometry: a robust, accurate, and single-shot measurement for objects with large depth discontinuities. Opt Express 2006;14(20):9178.
[92] Villa J, Araiza M, Alaniz D, Ivanov R, Ortiz M. Transformation of phase to (x,y,z)-coordinates for the calibration of a fringe projection profilometer. Opt Lasers Eng 2012;50(2):256–61.
[93] Wen Y, Li S, Cheng H, Su X, Zhang Q. Universal calculation formula and calibration method in Fourier transform profilometry. Appl Opt 2010;49(34):6563.
[94] Xu J, Douet J, Zhao J, Song L, Chen K. A simple calibration method for structured light-based 3D profile measurement. Optics & Laser Technology 2013;48:187–93.
[95] Zhou W-S, Su X-Y. A direct mapping algorithm for phase-measuring profilometry. J Mod Opt 1994;41(1):89–94.
[96] Zhan Song, Chung R. Use of LCD panel for calibrating structured-light-based range sensing system. IEEE Trans Instrum Meas 2008;57(11):2623–30.
[97] Falcao G, Hurtos N, Massich J. Plane-based calibration of a projector-camera system. VIBOT master 2008;9(1):1–12.
[98] Gao W, Wang L, Hu Z. Flexible method for structured light system calibration. Opt Eng 2008;47(8):083602.
[99] Huang J, Wang Z, Xue Q, Gao J. Calibration of a camera projector measurement system and error impact analysis. Meas Sci Technol 2012;23(12):125402.
[100] Din I, Anwar H, Syed I, Zafar H, Hasan L. Projector calibration for pattern projection systems. J Appl Res Technol 2014;12(1):80–6.
[101] Zhang X. Projector calibration from the camera image point of view. Opt Eng 2009;48(11):117208.
[102] Huang PS. Novel method for structured light system calibration. Opt Eng 2006;45(8):083601.
[103] Li Z. Accurate calibration method for a structured light system. Opt Eng 2008;47(5):053604.
[104] Xing S, Guo H. Iterative calibration method for measurement system having lens distortions in fringe projection profilometry. Opt Express 2020;28(2):1177.
[105] Liu K, Wang Y, Lau DL, Hao Q, Hassebrook LG. Dual-frequency pattern scheme for high-speed 3-Dshape measurement. Opt Express 2010;18(5):5229.
[106] Liu X, Cai Z, Yin Y, Jiang H, He D, He W, et al. Calibration of fringe projection profilometry using an inaccurate 2D reference target. Opt Lasers Eng 2017;89:131–7.
[107] Tian J, Ding Y, Peng X. Self-calibration of a fringe projection system using epipolar constraint. Optics & Laser Technology 2008;40(3):538–44.
[108] Jiang C, Lim B, Zhang S. Three-dimensional shape measurement using a structured light system with dual projectors. Appl Opt 2018;57(14):3983.
[109] Reich C. 3-D shape measurement of complex objects by combining photogrammetry and fringe projection. Opt Eng 2000;39(1):224.
[110] Yin Y, Peng X, Liu X, Li A, Qu X. Calibration strategy of optical measurement network for large-scale and shell-like objects. Opt Commun 2012;285(8):2048–56.
[111] Gai S, Da F, Tang M. A flexible multi-view calibration and 3D measurement method based on digital fringe projection. Meas Sci Technol 2019;30(2):025203.
[112] Legarda-Saenz R. Accurate procedure for the calibration of a structured light system. Opt Eng 2004;43(2):464.
[113] Huang Z, Xi J, Yu Y, Guo Q. Accurate projector calibration based on a new point–to-point mapping relationship between the camera and projector images. Appl Opt 2015;54(3):347.
[114] Chen R, Xu J, Chen H, Su J, Zhang Z, Chen K. Accurate calibration method for camera and projector in fringe patterns measurement system. Appl Opt 2016;55(16):4293.
[115] Notni GH, Notni G. Digital fringe projection in 3D shape measurement: an error analysis; 2003. p. 372. Munich, Germany
[116] Huang S, Xie L, Wang Z, Zhang Z, Gao F, Jiang X. Accurate projector calibration method by using an optical coaxial camera. Appl Opt 2015;54(4):789.
[117] Zhang W, Li W, Yu L, Luo H, Zhao H, Xia H. Sub-pixel projector calibration method for fringe projection profilometry. Opt Express 2017;25(16):19158.
[118] Chen R, Xu J, Zhang S, Chen H, Guan Y, Chen K. A self-recalibration method based on scale-invariant registration for structured light measurement systems. Opt Lasers Eng 2017;88:75–81.
[119] Schreiber W. Theory and arrangements of self-calibrating whole-body three--dimensional measurement systems using fringe projection technique. Opt Eng 2000;39(1):159.
[120] Liu M, Yang S, Wang Z, Huang S, Liu Y, Niu Z, et al. Generic precise augmented reality guiding system and its calibration method based on 3D virtual model. Opt Express 2016;24(11):12026.
[121] Moreno D, Taubin G. Simple, Accurate, and Robust Projector-Camera Calibration. In: 2012 second international conference on 3D imaging, modeling, processing, visualization & transmission. Zurich, Switzerland: IEEE; 2012. p. 464–71. ISBN 978-0-7695-4873-9 978-1-4673-4470-8
[122] Chen X, Xi J, Jin Y, Sun J. Accurate calibration for a camera projector measurement system based on structured light projection. Opt Lasers Eng 2009;47(3–4):310–19.
[123] Ma S, Zhu R, Quan C, Chen L, Tay CJ, Li B. Flexible structured-light-based three-dimensional profile reconstruction method considering lens projection-imaging distortion. Appl Opt 2012;51(13):2419.
[124] Chen C-Y, Chien H-J. An incremental target-adapted strategy for active geometric calibration of projector-camera systems. Sensors 2013;13(2):2664–81.
[125] Liu M, Sun C, Huang S, Zhang Z. An accurate projector calibration method based on polynomial distortion representation. Sensors 2015;15(10):26567–82.
[126] Chen C, Gao N, Zhang Z. Simple calibration method for dual-camera structured light system. Journal of the European Optical Society-Rapid Publications 2018;14(1):23.
[127] Juarez-Salazar R, Diaz-Ramirez VH. Flexible camera-projector calibration using superposed color checkerboards. Opt Lasers Eng 2019;120:59–65.
[128] Hu Y, Chen Q, Feng S, Zuo C. Microscopic fringe projection profilometry: areview. Opt Lasers Eng 2020:106192.
[129] Hu Y, Chen Q, Feng S, Tao T, Asundi A, Zuo C. A new microscopic telecentric stereo vision system - calibration, rectification, and three-dimensional reconstruction. Opt Lasers Eng 2019;113:14–22.
[130] Li B, Zhang S. Microscopic structured light 3D profilometry: binary defocusing technique vs. sinusoidal fringe projection. Opt Lasers Eng 2017;96:117–23.
[131] Peng J, Wang M, Deng D, Liu X, Yin Y, Peng X. Distortion correction for microscopic fringe projection system with scheimpflug telecentric lens. Appl Opt 2015;54(34):10055.
[132] Rao L, Da F, Kong W, Huang H. Flexible calibration method for telecentric fringe projection profilometry systems. Opt Express 2016;24(2):1222.
[133] Lu P, Sun C, Liu B, Wang P. Accurate and robust calibration method based on pattern geometric constraints for fringe projection profilometry. Appl Opt 2017;56(4):784.
[134] Vargas R, Marrugo AG, Zhang S, Romero LA. Hybrid calibration procedure for fringe projection profilometry based on stereo vision and polynomial fitting. Appl Opt 2020;59(13):D163.
[135] Chen L-C, Huang C-C. Miniaturized 3D surface profilometer using digital fringe projection. Meas Sci Technol 2005;16(5):1061–8.
[136] Chen L-C, Liao C-C. Calibration of 3D surface profilometry using digital fringe projection. Meas Sci Technol 2005;16(8):1554–66.
[137] Feng S, Chen Q, Zuo C, Sun J, Yu SL. High-speed real-time 3-D coordinates measurement based on fringe projection profilometry considering camera lens distortion. Opt Commun 2014;329:44–56.
[138] Huang S, Zhang Z, Zhao Y, Dai J, Chen C, Xu Y, et al. 3D Fingerprint imaging system based on full-field fringe projection profilometry. Opt Lasers Eng 2014;52:123–30.
[139] Huang J, Wu Q. A new reconstruction method based on fringe projection of three--dimensional measuring system. Opt Lasers Eng 2014;52:115–22.
[140] Vargas J. Flexible calibration procedure for fringe projection profilometry. Opt Eng 2007;46(2):023601.
[141] Vo M, Wang Z, Hoang T, Nguyen D. Flexible calibration technique for fringe-projection-based three-dimensional imaging. Opt Lett 2010;35(19):3192.
[142] Vo M, Wang Z, Pan B, Pan T. Hyper-accurate flexible calibration technique for fringe-projection-based three-dimensional imaging. Opt Express 2012;20(15):16926.
[143] Zappa E, Busca G, Sala P. Innovative calibration technique for fringe projection based 3D scanner. Opt Lasers Eng 2011;49(3):331–40.
[144] Zhang Z, Ma H, Zhang S, Guo T, Towers CE, Towers DP. Simple calibration of a phase-based 3D imaging system based on uneven fringe projection. Opt Lett 2011;36(5):627.
[145] Zhang Z, Huang S, Meng S, Gao F, Jiang X. A simple, flexible and automatic 3D calibration method for a phase calculation-based fringe projection imaging system. Opt Express 2013;21(10):12218.
[146] Chen C, Yu J, Gao N, Zhang Z. High accuracy 3D calibration method of phase calculation-based fringe projection system by using LCD screen considering refraction error. Opt Lasers Eng 2020;126:105870.
[147] Su X, Chen W. Reliability-guided phase unwrapping algorithm: a review. Opt Lasers Eng 2004;42(3):245–61.
[148] Zhao M, Huang L, Zhang Q, Su X, Asundi A, Kemao Q. Quality-guided phase unwrapping technique: comparison of quality maps and guiding strategies. Appl Opt 2011;50(33):6214.
[149] Chen L, Quan C. Fringe projection profilometry with nonparallel illumination: a least-squares approach. Opt Lett 2005;30(16):2101.
[150] Kofman J. Comparison of linear and nonlinear calibration methods for phase-measuring profilometry. Opt Eng 2007;46(4):043601.
[151] Zhang Z. A flexible new technique for camera calibration. IEEE Trans Pattern Anal Mach Intell 2000;22(11):1330–4.
[152] Tsai R. A versatile camera calibration technique for high-accuracy 3d machine vision metrology using off-the-shelf tv cameras and lenses. IEEE Journal on Robotics and Automation 1987;3(4):323–44.
[153] Heikkila J, Silvén O. A four-step camera calibration procedure with implicit image correction. In: Proceedings of IEEE computer society conference on computer vision and pattern recognition. IEEE; 1997. p. 1106–12.
[154] Camera calibration and 3D reconstruction - openCV. OpenCV https://docs.opencv.org/2.4/modules/calib3d/doc/camera_calibration_and_3d_reconstruction.html.
[155] Bouguet J.-Y. Camera calibration toolbox for matlab http://www.vision.caltech.edu/bouguetj/calib_doc/.
[156] Camera calibration and 3-D vision - MATLAB & simulink https://www.mathworks.com/help/vision/camera-calibration-and-3-d-vision.html.
[157] Tsai R. A versatile camera calibration technique for high-accuracy 3D machine vision metrology using off-the-shelf TV cameras and lenses. IEEE Journal on Robotics and Automation 1987;3(4):323–44.
[158] Cai Z, Liu X, Li A, Tang Q, Peng X, Gao BZ. Phase-3D mapping method developed from back-projection stereovision model for fringe projection profilometry. Opt Express 2017;25(2):1262.
[159] Sitnik R. Digital fringe projection system for large-volume 360-deg shape measurement. Opt Eng 2002;41(2):443.
[160] Yongchang Wang, Kai Liu, Qi Hao, Xianwang Wang, Lau DL, Hassebrook LG. Robust active stereo vision using kullback-leibler divergence. IEEE Trans Pattern Anal Mach Intell 2012;34(3):548–63.
[161] Zuo C, Chen Q, Gu G, Feng S, Feng F. High-speed three-dimensional profilometry for multiple objects with complex shapes. Opt Express 2012;20(17):19493.

[162] Wu Z, Guo W, Li Y, Liu Y, Zhang Q. High-speed and high-efficiency three--dimensional shape measurement based on Gray-coded light. Photonics Res 2020;8(6):819.
[163] Van der Jeught S, Dirckx JJ. Real-time structured light profilometry: a review. Opt Lasers Eng 2016;87:18–31.
[164] Zhang Z. Review of single-shot 3D shape measurement by phase calculation-based fringe projection techniques. Opt Lasers Eng 2012;50(8):1097–106.
[165] Huang L, Zhang Q, Asundi A. Flexible camera calibration using not-measured imperfect target. Appl Opt 2013;52(25):6278.
[166] Guo J, Peng X, Li A, Liu X, Yu J. Automatic and rapid whole-body 3D shape measurement based on multinode 3D sensing and speckle projection. Appl Opt 2017;56(31):8759.
[167] Liu X, Peng X, Chen H, He D, Gao BZ. Strategy for automatic and complete three--dimensional optical digitization. Opt Lett 2012;37(15):3126.
[168] Zhao H, Wang Z, Jiang H, Xu Y, Dong C. Calibration for stereo vision system based on phase matching and bundle adjustment algorithm. Opt Lasers Eng 2015;68:203–13.
[169] Goodfellow I, Bengio Y, Courville A, Bengio Y. Deep learning, 1. MIT press Cambridge; 2016.
[170] Voulodimos A, Doulamis N, Doulamis A, Protopapadakis E. Deep learning for computer vision: a brief review. Comput Intell Neurosci 2018;2018.
[171] Ioannidou A, Chatzilari E, Nikolopoulos S, Kompatsiaris I. Deep learning advances in computer vision with 3d data: a survey. ACM Computing Surveys (CSUR) 2017;50(2):1–38.
[172] Barbastathis G, Ozcan A, Situ G. On the use of deep learning for computational imaging. Optica 2019;6(8):921–43.
[173] Sinha A, Lee J, Li S, Barbastathis G. Lensless computational imaging through deep learning. Optica 2017;4(9):1117–25.
[174] Rivenson Y, Wu Y, Ozcan A. Deep learning in holography and coherent imaging. Light: Science & Applications 2019;8(1):1–8.
[175] Rivenson Y, Göröcs Z, Günaydin H, Zhang Y, Wang H, Ozcan A. Deep learning microscopy. Optica 2017;4(11):1437–43.
[176] Yan K, Yu Y, Huang C, Sui L, Qian K, Asundi A. Fringe pattern denoising based on deep learning. Opt Commun 2019;437:148–52.
[177] Li Z-w, Shi Y-s, Wang C-j, Qin D-h, Huang K. Complex object 3D measurement based on phase-shifting and a neural network. Opt Commun 2009;282(14):2699–706.
[178] Cuevas F, Servin M, Stavroudis O, Rodriguez-Vera R. Multi-layer neural network applied to phase and depth recovery from fringe patterns. Opt Commun 2000;181(4–6):239–59.
[179] Ganotra D, Joseph J, Singh K. Profilometry for the measurement of three-dimensional object shape using radial basis function, and multi-layer perceptron neural networks. Opt Commun 2002;209(4–6):291–301.
[180] Lv S, Sun Q, Zhang Y, Jiang Y, Yang J, Liu J, et al. Projector distortion correction in 3D shape measurement using a structured-light system by deep neural networks. Opt Lett 2020;45(1):204–7.